A Robust Nonlinear RLS Type Adaptive Filter for Second-Order-Intermodulation Distortion Cancellation in FDD LTE and 5G Direct Conversion Transceivers

Andreas Gebhard, *Student Member, IEEE*, Oliver Lang, *Member, IEEE*, Michael Lunglmayr, *Member, IEEE*, Christian Motz, *Student Member, IEEE*, Ram Sunil Kanumalli, *Student Member, IEEE*, Christina Auer, *Student Member, IEEE*, Thomas Paireder, Matthias Wagner, *Student Member, IEEE*, Harald Pretl, *Senior Member, IEEE*, and Mario Huemer, *Senior Member, IEEE*

***Abstract*— Transceivers operating in frequency division duplex experience a transmitter leakage (TxL) signal into the receiver due to the limited duplexer stopband isolation. This TxL signal in combination with the second-order nonlinearity of the receive mixer may lead to a baseband (BB) second-order intermodulation distortion (IMD2) with twice the transmit signal bandwidth. In direct conversion receivers, this nonlinear IMD2 interference may cause a severe signal-to-interference-plus-noise ratio degradation of the wanted receive signal. This contribution presents a nonlinear Wiener model recursive-least-squares (RLS) type adaptive filter for the cancellation of the IMD2 interference in the digital BB. The included channel-select filter and dc-notch filter at the output of the proposed adaptive filter ensure that the provided IMD2 replica includes the receiver front-end filtering. A second, robust version of the nonlinear recursive-least-squares (RLS) algorithm is derived which provides numerical stability for highly correlated input signals that arise in, e.g., Long-Term Evolution (LTE)-Advanced intra-band multi-cluster transmission scenarios. The performance of the proposed algorithms is evaluated by numerical simulations and by measurement data.**

***Index Terms*— Adaptive filters, 5G mobile communication, intermodulation distortion (IMD), interference cancellation, Long-Term Evolution (LTE)-Advanced.**

Manuscript received July 11, 2018; revised September 28, 2018 and December 21, 2018; accepted December 27, 2018. Date of publication February 27, 2019; date of current version May 6, 2019. The authors wish to acknowledge DMCE GmbH & Co KG as part of Intel for supporting this work carried out at the Christian Doppler Laboratory for Digitally Assisted RF Transceivers for Future Mobile Communications. The financial support by the Austrian Federal Ministry for Digital and Economic Affairs and the National Foundation for Research, Technology and Development is gratefully acknowledged. *(Corresponding author: Andreas Gebhard.)*

A. Gebhard, C. Motz, C. Auer, T. Paireder, M. Wagner, and M. Huemer are with the Christian Doppler Laboratory for Digitally Assisted RF Transceivers for Future Mobile Communications, Institute of Signal Processing, Johannes Kepler University Linz, 4040 Linz, Austria (e-mail: andreas.gebhard@jku.at).

O. Lang and M. Lunglmayr are with the Institute of Signal Processing, Johannes Kepler University Linz, 4040 Linz, Austria.

R. S. Kanumalli is with Danube Mobile Communications Engineering GmbH & Co KG as part of Intel, 4040 Linz, Austria.

H. Pretl is with the Institute for Integrated Circuits, Johannes Kepler University Linz, 4040 Linz, Austria.

Color versions of one or more of the figures in this paper are available online at http://ieeexplore.ieee.org.

Digital Object Identifier 10.1109/TMTT.2019.2896513

I. Introduction

MODERN radio frequency (RF) transceivers are enhanced by digital signal processing to mitigate non-idealities in the analog front end. One of the main reasons of receiver desensitization in frequency division duplex (FDD) transceivers is the limited duplexer isolation between the transmitter and the receiver which is around 50–55 dB [1], [2]. The resulting transmitter leakage (TxL) signal and the potentially leaking spurious intermodulation distortions (IMDs) caused by the nonlinear power amplifier (PA) in combination with receiver front-end nonlinearities (e.g., finite third-order input intercept point (IIP3) and second-order input intercept point (IIP2) [3]) of the low noise amplifier (LNA) and mixer may lead to additional IMDs, which can degrade the receiver performance [4]. Especially in carrier aggregation (CA) receivers, where the secondary receiver frequency is not coupled to the primary transmitter frequency, spurious IMDs of the PA may overlap the wanted receive signal of the secondary CA receiver [5]. Due to multiple clock sources, which are needed to cover different CA scenarios and band combinations, crosstalk between the receivers on the chip and device nonlinearities may create spurs in the receiver front end. If the frequency of such a spur falls near the actual transmit (Tx) frequency, the TxL signal may be down-converted into the receive (Rx) baseband (BB). This so-called modulated spur interference leads to a signal-to-noise ratio (SNR) degradation of the wanted receive signal [6]. Furthermore, the leaking transmitter signal may cause a IMD2 interference in direct-conversion receivers [7], [8]. The pure digital cancellation of this nonlinear IMD2 interference is presented in this paper. Besides the increasing costs, improving the Tx-to-Rx isolation of the duplexer would lead to a higher insertion loss of the wanted received signal and, thereby, to a reduction of the Rx signal quality. Therefore, instead of using improved duplexers, efficient ways to cancel the TxL signal and IMD caused receiver interferences are of special interest. In the existing literature, several approaches are discussed to mitigate

the TxL signal and PA spurious emission caused receiver desensitization. A natural approach would be to cancel the TxL signal in the RF domain before it enters the input of the LNA or mixer. This would significantly reduce the generation of nonlinear distortions due to receiver RF front-end nonlinearities. Kiayani *et al.* [9] propose an RF cancellation architecture using an auxiliary transmitter to generate a Tx leakage signal replica (including nonlinear PA distortions) in the RF domain which is subtracted from the received signal before it enters the LNA. The replica signal is generated by a nonlinear adaptive decorrelation-based learning algorithm, which uses the known Tx samples and the received signal in the digital BB. With this approach, the authors are able to increase the effective Tx-to-Rx isolation by 54 dB. A different way to suppress the leakage signal can be achieved by using N-path filters which act as a notch filter at the transmit frequency. In [2] and [10], such N-path filters are placed in front of the mixer input to reject the TxL signal. To limit the computational complexity of the pure digital modulated spur interference cancellation, Elmaghraby *et al.* [11] use an auxiliary receiver to sense the TxL signal at the receiver input, which is subsequently used as a reference signal for the digital cancellation algorithm. With this mixed-signal approach, the auxiliary receiver senses the Tx signal including nearby out-of-band (OOB) emissions after it passed the duplexer Tx-to-Rx stopband. This means that the duplexer stopband frequency response including the Tx OOB emissions is already included in the sensed TxL signal and does not need to be estimated by the digital algorithm. This heavily reduces the complexity of the digital part of the cancellation approach. The same auxiliary receiver could also be used to sense spurious emissions of the transmitter, which desensitize the receiver. However, nonlinearities of the receiver are not covered and need to be estimated by the digital cancellation algorithm. Using an auxiliary receiver with a serial-mixing concept to cancel the modulated spur interference [6], [12] including the phase noise (PN) of the involved transmitter and receiver local oscillators (LOs) is presented in [13]. Although analog and mixed-signal cancellation techniques offer good cancellation results as stated in [9], [11], and [13], their additional hardware effort is not negligible. Especially in CA, where multiple receiver chains are operated in parallel, each receiver (possibly including the diversity receivers) requires its own auxiliary receiver because of different duplexer stopband responses seen from the Tx to each receiver. A big challenge in designing analog or mixed-signal cancellation circuits is to limit the degradation of the wanted receive signal by connecting the auxiliary receiver [11], or transmitter [9] to the main receiver. Beside this, pure digital approaches offer technology independence and scalability and do not need any changes of the analog front-end circuit. However, the computational burden in the digital BB is increased.

In the existing literature, several fully digital techniques to cancel Tx-induced interferences can be found. Kiayani *et al.* [4] present the modeling and digital mitigation of transmitter self-interference in the presence of transmitter and receiver nonlinearities. In [14], the digital suppression of the nonlinear PA OOB emission which extends to the Rx band in the case of low duplexing distances is presented. The nonlinearity of the PA also induces spurious IMDs (Tx harmonics), which may degrade one of the CA receivers. The digital cancellation of such distortions in the presence of transmitter IQ-imbalance is suggested in [5]. The cancellation of the modulated spur interferences in CA transceivers by adaptive filtering is demonstrated in [6] and [12].

The main focus of this paper is the pure digital cancellation of the IMD2 interference. This second-order nonlinear distortion is caused by, e.g., a coupling between the RF- and LO-ports in the I-, and Q-path of the Rx IQ-mixer as indicated in Fig. 1 [15]. An interesting fact of this nonlinear interference is that one part of the generated second-order intermodulation products always falls around zero-frequency independent of the Tx-to-Rx frequency offset (duplexing distance). In the case of direct-conversion receiver architectures, this leads to a degradation of the wanted received signal.

The mathematical modeling in [7] and [8] shows that the BB IMD2 interference contains the squared envelope of the BB equivalent TxL signal. The resulting BB IMD2 interference has twice the Tx signal bandwidth and contains a dc due to the envelope-squaring. In the receiver front end, the overall dc arising from a number of sources is canceled by a mixed-signal cancellation to prevent the analog-to-digital converter (ADC) from saturation. In the digital domain, the signal is filtered by a channel-select filter (CSF) to reduce its bandwidth to the Long-Term Evolution (LTE) signal bandwidth.

In the existing literature, Lederer and Huemer [16], Frotzscher and Fettweis [17], and Kahrizi *et al.* [18] discussed adaptive least-mean-squares (LMS)-type IMD2 interference cancellation algorithms for frequency-flat duplexer stopbands. In [19], a Volterra kernel-based least-squares (LS) approach for frequency-selective Tx-to-Rx responses is proposed. Kiayani *et al.* [7] presented a two-step LS approach for the IMD2 cancellation and considered a static third-order PA nonlinearity and IQ-imbalance in the transmit mixer. In [20], a Tx CA transceiver is considered where the transmit signal of both transmitters leaks through a diplexer into one unpaired CA receiver. The diplexer stopband is modeled as a first-order finite impulse response (FIR) system which states a nearly frequency-flat response. The authors incorporated a fourth-order nonlinearity without memory into the estimation process, which results in an LS problem with four unknown coefficients.

This contribution presents a nonlinear Wiener model RLS-type adaptive filter (IM2RLS) with exponential forgetting factor, which is suitable for high-frequency-selective duplexer stopband frequency responses like indicated in Fig. 2. It targets the digital IMD2 cancellation for high-performance cellular base stations and mobile phones. The Wiener model uses a static nonlinearity at the output of the adaptive filter, which has the advantage that less coefficients are needed in the estimation process compared to a Volterra kernel-based adaptive filter [21].

An additional version of the proposed algorithm is presented, which enhances the algorithm by a dc-notch filter to cancel the dc in the interference replica. This is needed because direct-conversion receivers employ a dc cancellation

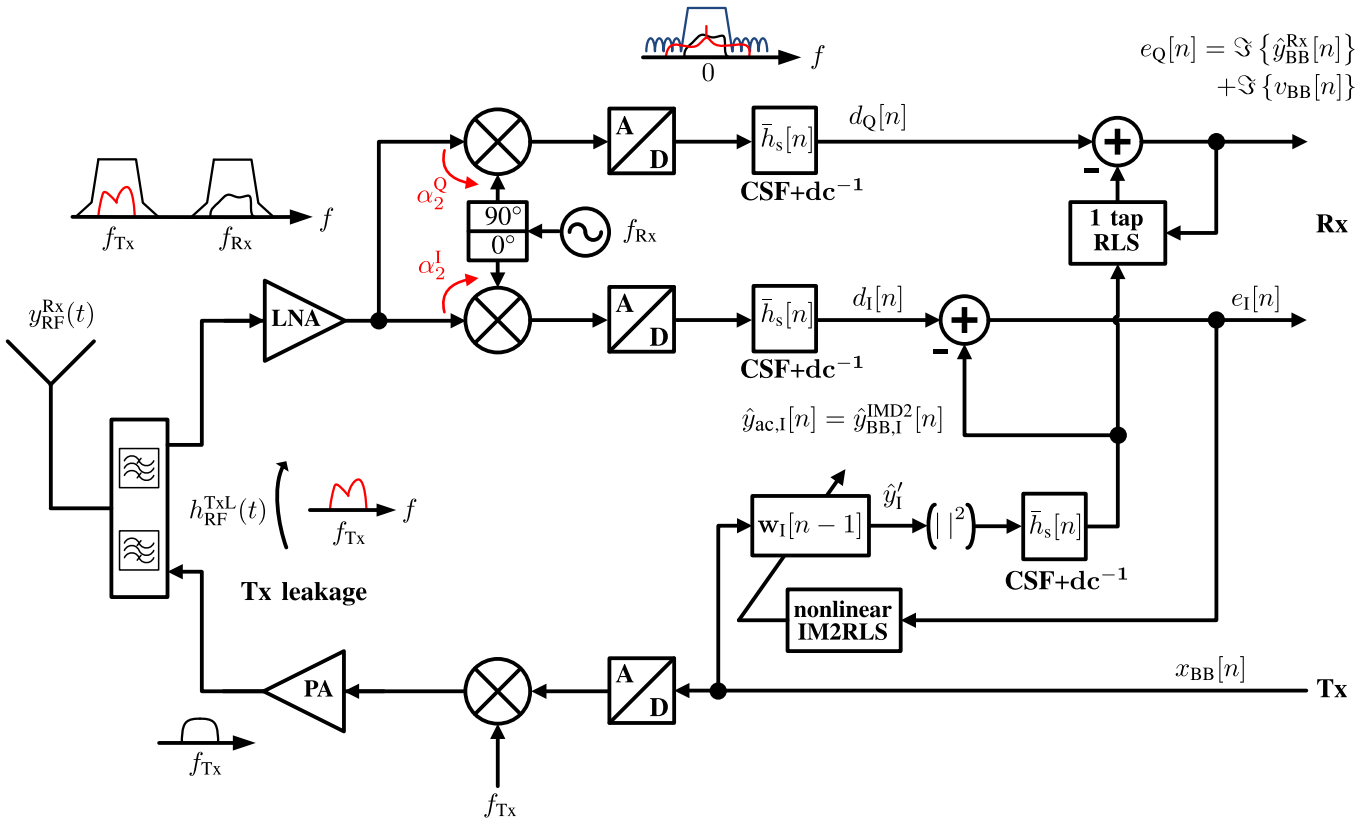

Fig. 1. Block diagram depicting an RF transceiver operating in FDD mode which experiences a second-order IMD in the receiver due to the TxL signal and the Rx mixer RF-to-LO terminal coupling. A nonlinear RLS-type adaptive filter is used to estimate the I-path IMD2 interference. The Q-path IMD2 interference is estimated with a linear 1-tap RLS adaptive filter, which uses the estimated I-path IMD2 replica as reference input.

to suppress the dc in order to prevent the ADC from saturation. The dc in the received signal is time variant and has many sources like, e.g., LO-LO self-mixing [15] and, therefore, must not be related explicitly to the dc which is generated by the IMD2 interference. Consequently, the IMD2 interference related dc is removed from the received signal, which complicates the IMD2 replica estimation. This dc removal is considered in [8] and [19] and neglected in [7], [16], [17], and [22].

The derived IM2RLS with dc-notch filter is extended by a regularization (R-IM2RLS), which makes the algorithm applicable for highly correlated BB transmit signals where the autocorrelation matrix can be close to singular. A high correlation in the transmit signal can be due to oversampling which happens, e.g., in the case of multi-cluster transmissions (introduced in the Third-Generation Partnership Project LTE-A Release 11) where only a part of the available resource blocks (RBs) are allocated. The presented IM2RLS algorithm is an extension to the nonlinear LMS-type adaptive filter derived in [8] with improved steady-state cancellation and convergence speed.

The structure of this paper is as follows. Section II explains the IIP2 characterization and demonstrates the degradation of the Rx performance due to the IMD2 interference. Section III provides a detailed IMD2 interference model, which motivates the proposed structure of the nonlinear adaptive filter. In Section IV, the IM2RLS algorithm is derived and the impact of adding a dc-notch filter to the algorithm is evaluated. The R-IM2RLS alrorithm is derived in Section V which is robust against highly correlated input signals as they occur in intra-band multi-cluster transmissions. Finally, in Sections VI and VII, the performance of the R-IM2RLS algorithm is evaluated with simulations and measured data using RF components.

II. Problem Statement

The receiver IIP2 is characterized by using two cosine signals with the frequencies f_1 and f_2 of equal amplitude and the total power $P_{\text{in,2t}}$ at the input of the nonlinear mixer. The resulting total IMD2 power in dBm generated at dc, $f_1 + f_2$, and $f_2 - f_1$ at the output of the mixer can be calculated by $P^{\text{Tot,2t}}_{\text{IM2}} = 2\ P_{\text{in,2t}} - \text{IIP2}$ [3]. Here, half of the total IMD2 power falls to dc, and one-quarter each to $f_1 + f_2$ and $f_2 - f_1$. To characterize the IIP2 in a zero-IF receiver, the frequencies f_1 and f_2 are chosen such that $f_2 - f_1$ falls within the CSF bandwidth. Thereby, the power $P^{f_2-f_1}_{\text{IM2}}$ at the frequency $f_2 - f_1$ is measured and the IIP2 is determined by $\text{IIP2} = 2\ P_{\text{in,2t}} - P^{f_2-f_1}_{\text{IM2}} - 6$ dB.

For modulated signals, the BB IMD2 power is modulation dependent and further reduced by the CSF. This is considered by a correction-factor, which corrects the IMD2 power calculated by the two-tone formula [23], [24].

Although the dc-filtering and channel-select filtering in the receiver reduce the IMD2 BB interference power by 6 dB in the two-tone signal case [3], and by about 13.4 dB [8], [23], [24] in the case of modulated Tx signals, the left-over IMD2 interference may lead to a severe SNR degradation of the wanted Rx signal in reference sensitivity

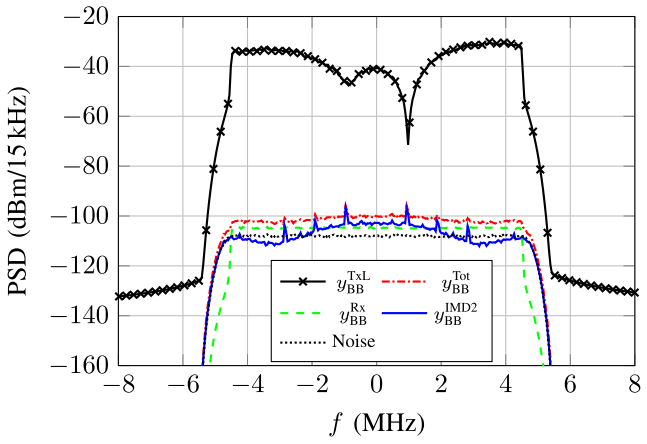

Fig. 2. Equivalent BB spectrum of the frequency-selective Tx leakage signal $y_{\mathrm{BB}}^{\mathrm{TxL}}$ (the corresponding passband signal is located at f_{Tx}) and the total received signal $y_{\mathrm{BB}}^{\mathrm{Tot}}$ after amplification with 20 dB LNA gain. The wanted Rx signal with SNR = 3 dB, and the receiver noise floor after amplification with 20 dB LNA gain are at −77 and −80 dBm $\widehat{=}$ −108.2 dBm/15 kHz respectively. The total received signal contains the dc-filtered, and channel-select filtered IMD2 interference with $P_{\mathrm{Tx}} = 23$ dBm at an assumed IIP2 of 50 dBm.

cases [25]. Assuming a transmitter power of 23 dBm at the antenna, and an average Tx-to-Rx duplexer isolation at the transmit frequency of 50 dB, the TxL signal power at the input of the receiver is $P_{\mathrm{RF}}^{\mathrm{TxL}} = 23\ \mathrm{dBm} - 50\ \mathrm{dB} = -27\ \mathrm{dBm}$. After amplification with the LNA gain which is assumed as 20 dB, the RF TxL signal power increases to $P_{\mathrm{RF}}^{\mathrm{TxL}} = -7\mathrm{dBm}$ at the input of the nonlinear mixer.

The IIP2 value of typical RF mixers is between 50 and 70 dBm [26], [27]. Assuming an IIP2 of 60 dBm, the resulting BB IMD2 power with a full allocated LTE10 QPSK modulated transmission and the determined correction factor of CF = 13.4 dB is $P_{\mathrm{IM2}}^{\mathrm{CSF,LTE}} = 2P_{\mathrm{RF}}^{\mathrm{TxL}} - \mathrm{IIP2} - \mathrm{CF} = -87.4$ dBm [8]. In an LTE10 reference sensitivity case, the wanted signal power at the antenna can be as low as −97 dBm [25]. The thermal noise power within 10 MHz bandwidth is −104.5 dBm, and the assumed receiver noise figure (NF) is 4.5 dB resulting in a receiver noise floor at −100 dBm. After amplification with 20 dB LNA gain, the wanted signal power is −77 dBm and the noise floor is at −80 dBm, which corresponds to a Rx SNR of 3 dB. The SNR drops from 3 dB to a signal-to-interference-plus-noise ratio (SINR) of 2.27 dB due to the IMD2 interference. In the case of a reduced IIP2 of 55 dBm/50 dBm, the SINR drops even further to 1 dB/−1.4 dB, respectively. Fig. 2 depicts the spectrum of the frequency-selective BB equivalent TxL signal $y_{\mathrm{BB}}^{\mathrm{TxL}}$, which generates the complex-valued IMD2 interference $y_{\mathrm{BB}}^{\mathrm{IMD2}}$ by a coupling between the RF-to-LO terminals of the I-, and Q-path mixer. The total received signal $y_{\mathrm{BB}}^{\mathrm{Tot}}$ contains the wanted Rx signal $y_{\mathrm{BB}}^{\mathrm{Rx}}$, which is degraded by the IMD2 interference and the noise.

III. System Model

A. IMD2 Interference Model

Based on the block diagram in Fig. 1 depicting an RF transceiver operating in FDD mode, a detailed IMD2 interference model is derived. The used mathematical operators $(.)^*$, $(.)^{\mathrm{T}}$, $(.)^{\mathrm{H}}$, and $*$ denote the complex conjugate, transpose, Hermitian transpose, and convolution, respectively. The complex BB transmit signal $x_{\mathrm{BB}}(t) = x_{\mathrm{I}}(t) + jx_{\mathrm{Q}}(t)$ is up-converted to the passband and amplified by the linearly assumed PA with gain A_{PA} resulting in the RF transmit signal

$$x_{\mathrm{RF}}(t) = A_{\mathrm{PA}}\Re\{x_{\mathrm{BB}}(t)e^{j2\pi f_{\mathrm{Tx}}t}\}. \tag{1}$$

This signal leaks through the duplexer RF stopband impulse response

$$h_{\mathrm{RF}}^{\mathrm{TxL}}(t) = 2\Re\left\{h_{\mathrm{BB}}^{\mathrm{TxL}}(t)e^{j2\pi f_{\mathrm{Tx}}t}\right\} \tag{2}$$

which is modeled by the BB equivalent duplexer impulse response $h_{\mathrm{BB}}^{\mathrm{TxL}}(t)$ into the receiver, thereby creating the TxL signal

$$\begin{aligned} y_{\mathrm{RF}}^{\mathrm{TxL}}(t) &= x_{\mathrm{RF}}(t) * h_{\mathrm{RF}}^{\mathrm{TxL}}(t) \\ &= A_{\mathrm{PA}}\Re\left\{\left[x_{\mathrm{BB}}(t) * h_{\mathrm{BB}}^{\mathrm{TxL}}(t)\right]e^{j2\pi f_{\mathrm{Tx}}t}\right\}. \end{aligned} \tag{3}$$

The received signal at the output of the LNA with gain A_{LNA}

$$y_{\mathrm{RF,LNA}}^{\mathrm{Tot}}(t) = A_{\mathrm{LNA}}\left[y_{\mathrm{RF}}^{\mathrm{TxL}}(t) + y_{\mathrm{RF}}^{\mathrm{Rx}}(t) + v_{\mathrm{RF}}(t)\right] \tag{4}$$

is composed by the amplified TxL signal, the wanted Rx signal $y_{\mathrm{RF}}^{\mathrm{Rx}}(t)$, and the noise signal $v_{\mathrm{RF}}(t)$. The output signal of the I-, and Q-path mixer is combined into the complex-valued signal $y_{\mathrm{RF,mixer}}^{\mathrm{Tot}}(t)$ (5). It contains the wanted signal, which is down-converted with the linear gains α_1^{I} and α_1^{Q}, and the second-order interference with the mixer RF-to-LO terminal coupling coefficient $\alpha_2 = \alpha_2^{\mathrm{I}} + j\alpha_2^{\mathrm{Q}}$

$$\begin{aligned} y_{\mathrm{RF,mixer}}^{\mathrm{Tot}}(t) &= y_{\mathrm{RF,LNA}}^{\mathrm{Tot}}(t)\alpha_1^{\mathrm{I}}\cos(2\pi f_{\mathrm{Rx}}t) \\ &\quad + y_{\mathrm{RF,LNA}}^{\mathrm{Tot}}(t)\left[\alpha_2^{\mathrm{I}}y_{\mathrm{RF,LNA}}^{\mathrm{Tot}}(t)\right] \\ &\quad - jy_{\mathrm{RF,LNA}}^{\mathrm{Tot}}(t)\alpha_1^{\mathrm{Q}}\sin(2\pi f_{\mathrm{Rx}}t) \\ &\quad + jy_{\mathrm{RF,LNA}}^{\mathrm{Tot}}(t)\left[\alpha_2^{\mathrm{Q}}y_{\mathrm{RF,LNA}}^{\mathrm{Tot}}(t)\right] \\ &= y_{\mathrm{RF,LNA}}^{\mathrm{Tot}}(t)\alpha_1 e^{-j2\pi f_{\mathrm{Rx}}t} + \alpha_2\ y_{\mathrm{RF,LNA}}^{\mathrm{Tot}}(t)^2. \end{aligned} \tag{5}$$

Assuming a direct conversion receiver, and using the identity $\Re\{\eta e^{j\kappa}\} = 1/2(\eta e^{j\kappa} + \eta^* e^{-j\kappa})$, the total mixer output signal by neglecting the signal content which falls outside the BB bandwidth becomes (with $\alpha_1 = \alpha_1^{\mathrm{I}} = \alpha_1^{\mathrm{Q}}$)

$$\begin{aligned} y_{\mathrm{RF,mixer}}^{\mathrm{Tot}}(t) &= \alpha_1\frac{A_{\mathrm{LNA}}}{2}y_{\mathrm{BB}}^{\mathrm{Rx}}(t) + \alpha_1\frac{A_{\mathrm{LNA}}}{2}v_{\mathrm{BB}}(t) \\ &\quad + \frac{\alpha_2 A_{\mathrm{LNA}}^2}{2}\left[\left|A_{\mathrm{PA}}\,x_{\mathrm{BB}}(t) * h_{\mathrm{BB}}^{\mathrm{TxL}}(t)\right|^2 + \left|y_{\mathrm{BB}}^{\mathrm{Rx}}(t)\right|^2\right. \\ &\quad \left. + 2\Re\left\{y_{\mathrm{BB}}^{\mathrm{Rx}}(t)v_{\mathrm{BB}}^*(t)\right\} + |v_{\mathrm{BB}}(t)|^2\right]. \end{aligned} \tag{6}$$

As in critical, e.g., cell edge scenarios the Rx and noise signal are much weaker than the TxL signal, the last three terms in (6) may be neglected [7], [8]. The total received discrete-time BB signal

$$\begin{aligned} y_{\mathrm{BB}}^{\mathrm{Tot}}[n] &= \alpha_1\frac{A_{\mathrm{LNA}}}{2}y_{\mathrm{BB}}^{\mathrm{Rx}}[n] * \bar{h}_s[n] + \alpha_1\frac{A_{\mathrm{LNA}}}{2}v_{\mathrm{BB}}[n] * \bar{h}_s[n] \\ &\quad + \underbrace{\frac{\alpha_2}{2}\left|A_{\mathrm{LNA}}A_{\mathrm{PA}}x_{\mathrm{BB}}[n] * h_{\mathrm{BB}}^{\mathrm{TxL}}[n]\right|^2 * \bar{h}_s[n]}_{y_{\mathrm{BB}}^{\mathrm{IMD2}}[n]} \end{aligned} \tag{7}$$

contains the BB IMD2 interference $y_{\mathrm{BB}}^{\mathrm{IMD2}}[n]$ and includes the dc cancellation and channel-select filtering which are combined in the impulse response $\bar{h}_s[n] = h_{\mathrm{dc}}[n] * h_s[n]$. Here, $h_{\mathrm{BB}}^{\mathrm{TxL}}[n] = T_s h_{\mathrm{BB}}^{\mathrm{TxL}}(t)\big|_{t=nT_s}$ is the impulse invariant [28], [29], scaled and sampled version of the continuous-time BB duplexer impulse response $h_{\mathrm{BB}}^{\mathrm{TxL}}(t)$.

B. Interference Replica Model

For the adaptive filter development to cancel the IMD2 interference in the digital BB, the interference model (7) is rewritten to the form

$$y_{\mathrm{BB}}^{\mathrm{Tot}}[n] = \underbrace{\frac{\alpha_2^{\mathrm{I}}}{2}\left|A_{\mathrm{LNA}}A_{\mathrm{PA}}x_{\mathrm{BB}}[n] * h_{\mathrm{BB}}^{\mathrm{TxL}}[n]\right|^2 * \bar{h}_s[n]}_{y_{\mathrm{BB}}^{\mathrm{IMD2,I}}[n]} + j\underbrace{\frac{\alpha_2^{\mathrm{Q}}}{2}\left|A_{\mathrm{LNA}}A_{\mathrm{PA}}x_{\mathrm{BB}}[n] * h_{\mathrm{BB}}^{\mathrm{TxL}}[n]\right|^2 * \bar{h}_s[n]}_{y_{\mathrm{BB}}^{\mathrm{IMD2,Q}}[n]} + v'_{\mathrm{BB}}[n] \tag{8}$$

where the complex-valued wanted signal and the noise signal are combined in $v'_{\mathrm{BB}}[n]$. Assuming $\alpha_2^{\mathrm{I}} > 0$, and approximating the duplexer impulse response $h_{\mathrm{BB}}^{\mathrm{TxL}}[n]$ by the FIR impulse response vector $\mathbf{h}_{\mathrm{BB}}^{\mathrm{TxL}}$ of length $N_{\mathbf{h}}$, we can rewrite the model (8) further to

$$\begin{aligned} y_{\mathrm{BB}}^{\mathrm{Tot}}[n] &= |\mathbf{x}^{\mathrm{T}}[n]\mathbf{h}_{\mathrm{I}}|^2 * \bar{h}_s[n] + j|\mathbf{x}^{\mathrm{T}}[n]\mathbf{h}_{\mathrm{Q}}|^2 * \bar{h}_s[n] + v'_{\mathrm{BB}}[n] \\ &= y_{\mathrm{BB}}^{\mathrm{IMD2,I}}[n] + j\epsilon\ y_{\mathrm{BB}}^{\mathrm{IMD2,I}}[n] + v'_{\mathrm{BB}}[n] \end{aligned} \tag{9}$$

where $\mathbf{h}_{\mathrm{I}}$ and $\mathbf{h}_{\mathrm{Q}}$ are incorporating $\mathbf{h}_{\mathrm{BB}}^{\mathrm{TxL}}$ and all scalar scaling factors in the I-, and Q-path, respectively. The used vector $\mathbf{x}[n]$ is the complex-valued tapped delay-line input signal vector $\mathbf{x}[n] = [x_{\mathrm{BB}}[n], x_{\mathrm{BB}}[n-1], \ldots, x_{\mathrm{BB}}[n - N_{\mathbf{h}} + 1]]^{\mathrm{T}}$, and the real-valued scaling factor ϵ shows that the Q-path IMD2 interference may be modeled as a scaled version of the I-path interference. Motivated by the model (9), we propose the I-path IMD2 interference replica model

$$\hat{y}_{\mathrm{ac,I}}[n] = |\mathbf{x}^{\mathrm{T}}[n]\mathbf{w}_{\mathrm{I}}[n]|^2 * \bar{h}_s[n] \tag{10}$$

using the adaptive filter coefficient vector $\mathrm{w}_{\mathrm{I}}[n]$ and delay-line input vector $\mathbf{x}[n]$ of length $N_{\mathbf{w}}$. The index ac indicates the dc cancellation in the IMD2 replica generation. The replica model comprises an adaptive Wiener model FIR filter where the output signal is dc-filtered, and channel-select filtered. The Q-path IMD2 interference is generated by estimating the scaling parameter ϵ by a linear single-tap RLS algorithm, which uses the estimated I-path IMD2 interference as reference input. This model is used to derive the adaptive filter structure shown in Fig. 1 to cancel the IMD2 interference in the digital BB. For the case if $\alpha_2^{\mathrm{I}} < 0$, the sign of the desired signal in the I-path d_{I} and the replica signal of the adaptive filter need to be changed.

IV. Nonlinear Recursive LS Algorithm

In this section, a nonlinear Wiener model RLS-type adaptive filter to estimate the channel-select filtered I-path IMD2 interference is developed. In a first step, the IM2RLS algorithm without dc-notch filter, which implies that the received signal contains the dc, is developed. Therefore, the replica model (10) without dc cancellation

$$\begin{aligned} \hat{y}_{\mathrm{I}}[n] &= |\mathbf{x}^{\mathrm{T}}[n]\mathbf{w}_{\mathrm{I}}[n]|^2 * h_s[n] \\ &= \mathbf{x}^{\mathrm{T}}[n]\mathbf{w}_{\mathrm{I}}[n]\mathbf{x}^{\mathrm{H}}[n]\mathbf{w}_{\mathrm{I}}^*[n] * h_s[n] \end{aligned} \tag{11}$$

is used. The LS cost function up to the time index n with the exponential forgetting factor $0 \ll \lambda \leq 1$ is

$$J_{\mathrm{LS}}[n] = \sum_{i=0}^{n} \lambda^{n-i}\left|d_{\mathrm{I}}[i] - \mathbf{x}^{\mathrm{T}}[i]\mathbf{w}_{\mathrm{I}}[n]\mathbf{x}^{\mathrm{H}}[i]\mathbf{w}_{\mathrm{I}}^*[n] * h_s[i]\right|^2. \tag{12}$$

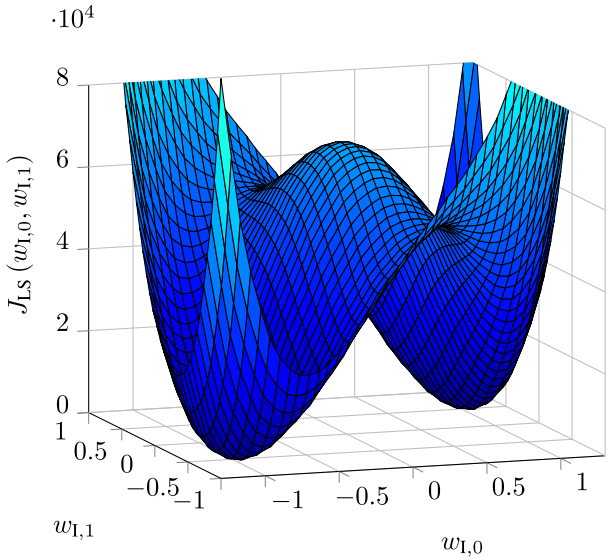

Fig. 3. Shape of the cost function (12) for white Gaussian input signals with $\lambda = 1$ and for the real-valued coefficient vector $\mathbf{h}_{\mathrm{I}} = [1, 0.5]^{\mathrm{T}}$ when the desired signal $d_{\mathrm{I}}[n]$ and the IMD2 replica are containing the dc. At the origin $\mathbf{w}_{\mathrm{I}} = \mathbf{0}$, a local maximum can be observed.

This cost function is visualized in Fig. 3, for the example impulse response $\mathbf{h}_{\mathrm{I}} = [1, 0.5]^{\mathrm{T}}$ and $\lambda = 1$ where the estimated coefficients $w_{\mathrm{I},0}$ and $w_{\mathrm{I},1}$ are constrained to be real-valued. Two equivalent global minimum points and a local maximum at the origin $\mathbf{w}_{\mathrm{I}} = \mathbf{0}$ can be observed. The two solutions $\mathbf{w}_{\mathrm{I},1} = [1, 0.5]^{\mathrm{T}}$, and $\mathbf{w}_{\mathrm{I},2} = [-1, -0.5]^{\mathrm{T}}$ minimize the cost function which can be explained with the absolute-squaring nature of the IMD2 interference. Both solutions lead to the same IMD2 replica signal. Assuming real-valued CSF impulse response coefficients $h_s[n]$, and observing that $d_{\mathrm{I}}[i]$ is the desired signal in the I-path, and therefore, real-valued, the gradient of the cost function (12) may be derived. The gradient of the cost function with respect to the coefficient vector $\mathbf{w}_{\mathrm{I}}$ using the Wirtinger calculus [30]–[32] becomes

$$\begin{aligned} \nabla_{\mathbf{w}_{\mathrm{I}}} J_{\mathrm{LS}} &= 2\left[\frac{\partial J_{\mathrm{LS}}[n]}{\partial \mathbf{w}_{\mathrm{I}}^*[n]}\right]^{\mathrm{T}} \\ &= 2\sum_{i=0}^{n} \lambda^{n-i}\big[-2\,d_{\mathrm{I}}[i]\mathbf{x}^{\mathrm{T}}[i]\mathbf{w}_{\mathrm{I}}[n]\mathbf{x}^*[i] * h_s[i] \\ &\qquad + 2(\mathbf{x}^{\mathrm{T}}[i]\mathbf{w}_{\mathrm{I}}[n]\mathbf{x}^*[i] * h_s) \\ &\qquad \cdot \left(\mathbf{x}^{\mathrm{H}}[i]\mathbf{w}_{\mathrm{I}}^*[n]\mathbf{x}^{\mathrm{T}}[i] * h_s[i]\right)\mathbf{w}_{\mathrm{I}}[n]\big]. \end{aligned} \tag{13}$$

By setting the gradient to zero, the Wiener Filter equation is obtained by

$$\tilde{\mathbf{R}}(\mathbf{w}_\mathrm{I}[n])\mathbf{w}_\mathrm{I}[n] = \tilde{\mathbf{r}}(\mathbf{w}_\mathrm{I}[n]) \tag{14}$$

where it can be observed that the autocorrelation matrix $\tilde{\mathbf{R}}$ and the cross-correlation vector $\tilde{\mathbf{r}}$ are functions of the unknown coefficient vector $\mathbf{w}_\mathrm{I}[n]$. In a slowly varying or nearly stationary system environment, it can be assumed that $\mathbf{x}^\mathrm{T}[i]\mathbf{w}_\mathrm{I}[n] \approx \mathbf{x}^\mathrm{T}[i]\mathbf{w}_\mathrm{I}[i-1]$ when the index i is close to n [33], [34]. If the index $i \ll n$, the approximation introduces an error, which is, however, attenuated by the forgetting factor. Defining the new cost function

$$\begin{aligned} J'_{\mathrm{LS}}[n] &= \sum_{i=0}^{n} \lambda^{n-i} \left| d_\mathrm{I}[i] - \mathbf{x}^\mathrm{T}[i]\mathbf{w}_\mathrm{I}[i-1]\mathbf{x}^\mathrm{H}[i]\mathbf{w}_\mathrm{I}^*[n] * h_s[i] \right|^2 \\ &= \sum_{i=0}^{n} \lambda^{n-i} \left| d_\mathrm{I}[i] - \mathbf{z}^\mathrm{T}[i]\mathbf{w}_\mathrm{I}^*[n] * h_s[i] \right|^2 \\ &= \sum_{i=0}^{n} \lambda^{n-i} \, |e_\mathrm{I}[i]|^2 \end{aligned} \tag{15}$$

and introducing the new input vector $\mathbf{z}[i] = \mathbf{x}^\mathrm{T}[i]\mathbf{w}_\mathrm{I}[i-1]\mathbf{x}^*[i]$, we can overcome this limitation. Following the traditional RLS derivation [35], the IM2RLS algorithm to estimate the I-path IMD2 interference in the digital BB becomes the following:

$$\hat{y}_\mathrm{I}[n] = \mathbf{z}^\mathrm{T}[n]\mathbf{w}_\mathrm{I}^*[n-1] * h_s[n] \tag{16}$$

$$e_\mathrm{I}[n] = d_\mathrm{I}[n] - \hat{y}_\mathrm{I}[n] \tag{17}$$

$$\mathbf{k}[n] = \frac{\mathbf{P}[n-1]\mathbf{z}_\mathrm{f}[n]}{\lambda + \mathbf{z}_\mathrm{f}^\mathrm{H}[n]\mathbf{P}[n-1]\mathbf{z}_\mathrm{f}[n]} \tag{18}$$

$$\mathbf{P}[n] = \frac{1}{\lambda}\left[\mathbf{P}[n-1] - \mathbf{k}[n]\mathbf{z}_\mathrm{f}^\mathrm{H}[n]\mathbf{P}[n-1]\right] \tag{19}$$

$$\mathbf{w}_\mathrm{I}[n] = \mathbf{w}_\mathrm{I}[n-1] + e_\mathrm{I}[n]\mathbf{k}[n]. \tag{20}$$

To avoid the channel-select filtering of each element in the vector $\mathbf{z}_\mathrm{f}[n] = \mathbf{z}[n] * h_s[n]$, which is mainly necessary to align the signals due to the CSF group delay, we introduce the signals $x_\mathrm{f}[n] = x_\mathrm{BB}[n] * h_s[n]$ and $y'_\mathrm{I}[n] = \mathbf{x}^\mathrm{T}[n]\mathbf{w}_\mathrm{I}[n-1]$. Using the delay line vector $\mathbf{x}_\mathrm{f}[n] = [x_\mathrm{f}[n], x_\mathrm{f}[n-1], \ldots, x_\mathrm{f}[n-M+1]]^\mathrm{T}$, the vector $\mathbf{z}_\mathrm{f}[n]$ may be approximated by $\mathbf{z}_\mathrm{f}[n] \approx (y'_\mathrm{I}[n] * h_s[n])\mathbf{x}_\mathrm{f}^*[n]$. With this formulation, a fractional and nonconstant group delay of the CSF may be incorporated. In case if the group delay τ_g is constant, and an integer multiple of the sampling time (as e.g., in linear phase FIR filters), the CSF may be approximated by delaying the signal by $\mathbf{z}_\mathrm{f}[n] \approx \mathbf{x}^\mathrm{T}[n-\tau_g]\mathbf{w}_\mathrm{I}[n-1-\tau_g]\mathbf{x}^*[n-\tau_g]$. In both approximations, the band-limiting effect of the CSF on $\mathbf{z}_\mathrm{f}[n]$ is ignored. However, this may be tolerated because due to the envelope-squaring operation in (11) which doubles the signal bandwidth, anyhow an oversampling factor (OSF) of 2 is mandatory to avoid aliasing. Due to the fact that the I-, and Q-path IMD2 interferences differ only by a real-valued scaling factor ϵ as derived in (8), the estimated I-path IMD2 replica may be used as a reference to estimate the Q-path IMD2 replica. This may be done by a linear 1-tap RLS algorithm, which uses the estimated I-path replica as a reference input signal to estimate the Q-path IMD2 replica. In this case, the 1-tap RLS estimates also a possible sign difference between the I-, and Q-path IMD2 interference. Consequently, only the sign of α_2^I has to be detected during the calibration of the receiver, which may be done by correlation. The replica signal generation (16) is channel-select filtered, which reduces the bandwidth of the replica signal to the bandwidth of the received LTE signal.

A. Second-Order Condition

The complex Hessian [31], [36] of the cost function (12) at the coefficient value $\mathbf{w}_\mathrm{I} = \mathbf{0}$ becomes

$$\begin{aligned} H_\mathrm{I} &= \frac{\partial}{\partial \mathbf{w}_\mathrm{I}} \left[\frac{\partial J_\mathrm{LS}}{\partial \mathbf{w}_\mathrm{I}^*} \right]^\mathrm{T} |_{\mathbf{w}_\mathrm{I}=\mathbf{0}} \\ &= \sum_{i=0}^{n} \lambda^{n-i} [-2\, d_\mathrm{I}[i]\mathbf{x}^*[i]\mathbf{x}^\mathrm{T}[i] * h_s[i]]. \end{aligned} \tag{21}$$

If the desired signal $d_\mathrm{I}[n]$ contains the dc (when the receiver has no dc filtering), then $E\{d_\mathrm{I}[n]\} \geq 0$ and the Hessian matrix becomes negative semidefinite like depicted with the local maximum in Fig. 3. The usual choice of the zero-vector as initialization of $\mathbf{w}_\mathrm{I}[-1]$ results in a zero-gain vector $\mathbf{k}[n]$ for all n. This is reasoned in the cost function (12) depicted in Fig. 3 which has a local maximum at $\mathbf{w}_\mathrm{I} = \mathbf{0}$ and, therefore, a vanishing gradient. Consequently, the algorithm is initialized with $\mathbf{w}_\mathrm{I}[-1] \neq \mathbf{0}$ and the parameters $0 \ll \lambda \leq 1$, and $\mathbf{P}[-1] = \nu\, \mathbf{I}$ with $\nu > 0$. If no prior knowledge about the Tx-to-Rx leakage channel is available, an initialization close to the zero-vector, e.g., $\mathbf{w}_\mathrm{I}[-1] = [10^{-6}, 0, 0, \ldots, 0]^\mathrm{T}$ is a reasonable choice. For a practical implementation we suggest to initialize the first entry of $\mathbf{w}_\mathrm{I}[-1]$ with the smallest representable number that is larger than zero.

B. DC Cancellation

To employ an IMD2 interference replica without dc, the replica signal (16) is filtered by the dc-notch filter (23). The new error signal $e_{\mathrm{ac,I}}[n] = d_{\mathrm{ac,I}}[n] - \hat{y}_{\mathrm{ac,I}}[n]$ with the dc-filtered signals is used in the update (27). Here, the introduced index ac indicates the dc filtered signals. The IM2RLS algorithm with dc-suppression can be summarized as follows:

$$\hat{y}_\mathrm{I}[n] = \mathbf{z}^\mathrm{T}[n]\mathbf{w}_\mathrm{I}^*[n-1] * h_s[n] \tag{22}$$

$$\hat{y}_{\mathrm{ac,I}}[n] = a\, \hat{y}_{\mathrm{ac,I}}[n-1] + \hat{y}_\mathrm{I}[n] - \hat{y}_\mathrm{I}[n-1] \tag{23}$$

$$e_{\mathrm{ac,I}}[n] = d_{\mathrm{ac,I}}[n] - \hat{y}_{\mathrm{ac,I}}[n] \tag{24}$$

$$\mathbf{k}[n] = \frac{\mathbf{P}[n-1]\mathbf{z}_\mathrm{f}[n]}{\lambda + \mathbf{z}_\mathrm{f}^\mathrm{H}[n]\mathbf{P}[n-1]\mathbf{z}_\mathrm{f}[n]} \tag{25}$$

$$\mathbf{P}[n] = \frac{1}{\lambda}\left[\mathbf{P}[n-1] - \mathbf{k}[n]\mathbf{z}_\mathrm{f}^\mathrm{H}[n]\mathbf{P}[n-1]\right] \tag{26}$$

$$\mathbf{w}_\mathrm{I}[n] = \mathbf{w}_\mathrm{I}[n-1] + e_{\mathrm{ac,I}}[n]\mathbf{k}[n]. \tag{27}$$

The parameter $0 \ll a < 1$ in (23) determines the sharpness of the dc-notch filter and is chosen as $a = 0.998$. In the case of dc filtering in the main receiver $E\{d_\mathrm{I}[n]\} = 0$, and the Hessian matrix (21) at $\mathbf{w}_\mathrm{I} = \mathbf{0}$ is not positive semidefinite anymore. In this case, the local maximum becomes a saddle point like depicted in Fig. 4. Using N_CSF as the number

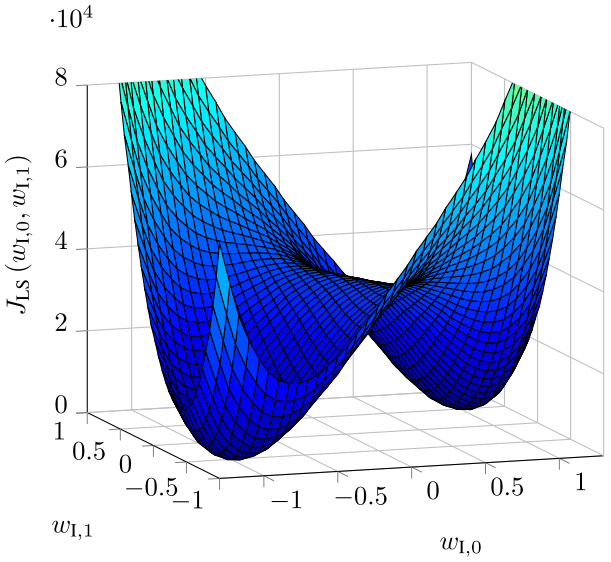

Fig. 4. Shape of the cost function (12) for white Gaussian input signals with $\lambda = 1$ and for the two real-valued coefficients $\mathbf{h}_{\mathrm{I}} = [1, 0.5]^{\mathrm{T}}$. The local maximum at $\mathbf{w}_{\mathrm{I}} = \mathbf{0}$ (with dc) changed to a saddle point because the dc filtering is applied.

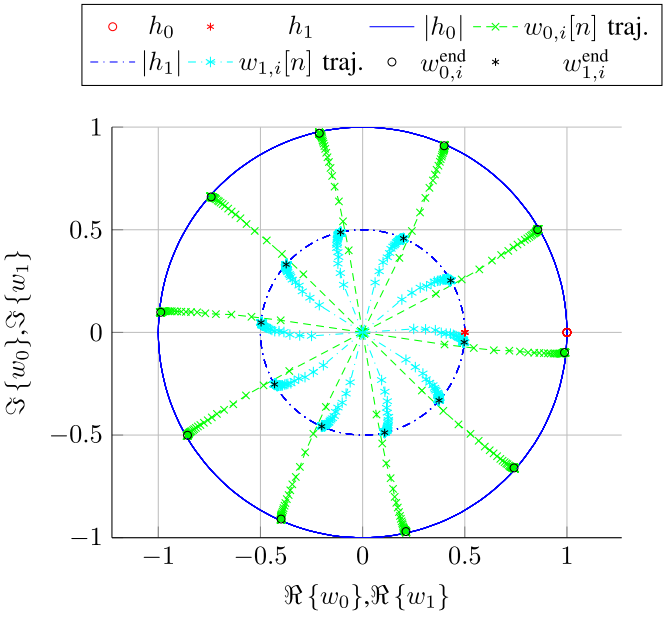

Fig. 5. Illustration of the initialization-dependent multiple solutions where the true coefficient values are $\mathbf{h}_{\mathrm{I}} = [1, 0.5]^{\mathrm{T}}$. The initial coefficient $w_0[-1]$ is initialized in a ten-point grid around a circle with radius 1×10^{-3}. The initial value of $w_1[-1]$ is always zero. With each initialization, the coefficients converge to the correct absolute value. All ten resulting estimated impulse response vectors $\mathbf{w}_i^{\mathrm{end}}$ maintain the same group delay as $\mathbf{h}_{\mathrm{I}}$.

of coefficients in the CSF difference equation, the computational complexity of the IM2RLS with dc-notch filter is $13N_{\mathbf{w}}^2 + 5N_{\mathrm{CSF}} + 20N_{\mathbf{w}} + 1$ real multiplications and 2 $N_{\mathbf{w}}$ real divisions per iteration.

C. Multiple Solutions of the IM2RLS Algorithm

In the cost function shapes depicted in Figs. 3 and 4, the estimated impulse response coefficients w_0 and w_1 (omitting the index I for the I-path) are constrained to be real-valued. It can be observed that the two solutions $\mathbf{w}_0 = [1, 0.5]^{\mathrm{T}}$, and $\mathbf{w}_1 = [-1, -0.5]^{\mathrm{T}}$ minimize the cost function. The existence of multiple solutions can be explained by the absolute-squaring nature of the IMD2 interference.

If the coefficients are allowed to be complex-valued, all coefficient pairs $\{w_0, w_1\}$ converge to $|w_0^{\mathrm{end}}| = |h_0|$ and $|w_1^{\mathrm{end}}| = |h_1|$. This scenario is visualized in Fig. 5 where the convergence of the coefficients with ten different initializations $\mathbf{w}_i[-1] = [10^{-3}, 0]^{\mathrm{T}} \exp(j2\pi/10\, i)$ for $i = 0 \ldots 9$ is depicted. Furthermore, each of the estimated coefficient vectors $\mathbf{w}_i^{\mathrm{end}} = [w_{0,i}^{\mathrm{end}}, w_{1,i}^{\mathrm{end}}]^{\mathrm{T}}$ after convergence reach the group delay of the real system impulse response $\mathbf{h}_{\mathrm{I}}$.

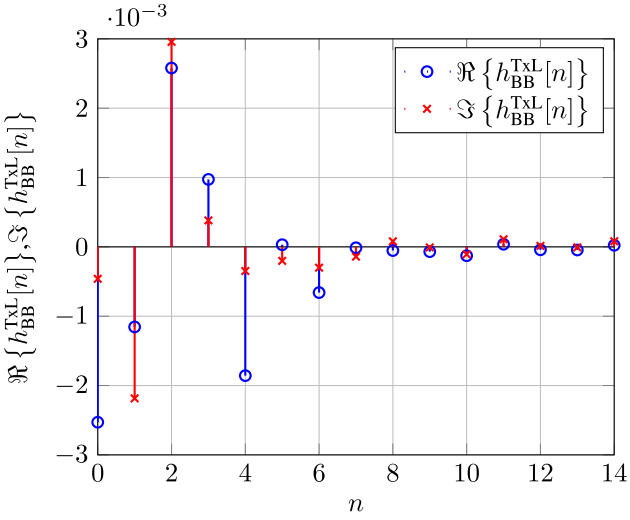

Fig. 6. Real and imaginary parts of the 15-tap complex-valued duplexer impulse response.

D. Performance of the IM2RLS With DC Suppression

In this section, the performance of the IM2RLS w/o and w/ dc cancellation is compared. In the first case, the receiver and the IMD2 replica generation of the IM2RLS do not use a dc cancellation. In this hypothetical example, it is assumed that the IMD2 interference is the only dc source. In the second case, the receiver uses a dc suppression, and the IM2RLS uses the dc-notch filter. Both cases are compared within a FDD scenario with full-allocated Long Term Evolution (LTE) signals using 10 MHz bandwidth, QPSK modulation, short cyclic prefix, and an OSF of 2. The frequency-selective duplexer stopband impulse response shown in Fig. 6 is used in (7) for the IMD2 interference generation. It is modeled with an FIR system which has 15 complex-valued coefficients (on the native LTE10 sampling rate of 15.36 MHz) and a mean Tx-to-Rx isolation of 50 dB [1]. The resulting TxL signal has a strong frequency-selectivity like indicated in Fig. 2. The wanted Rx signal power is at reference sensitivity level $P_{\mathrm{Rx}} = -97$ dBm and the thermal noise floor is -104.5 dBm within 10 MHz bandwidth. The receiver NF is 4.5 dB which results in an receiver noise floor of -100 dBm. The LNA gain is 20 dB, and the two-tone mixer IIP2 is

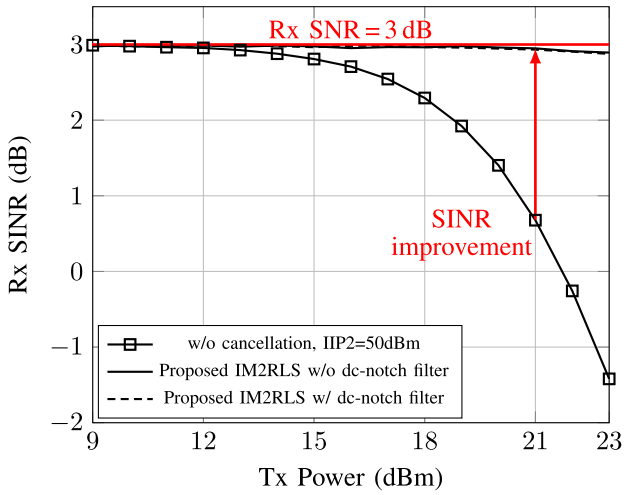

Fig. 7. Improvement of the Rx SINR with the proposed IMD2 cancellation algorithms w/o and w/ using the dc-notch filter at different transmitter power levels. The mixer IIP2 is 50 dBm and the wanted signal at the antenna has a power of P_{Rx} =-97 dBm and an SNR of 3 dB.

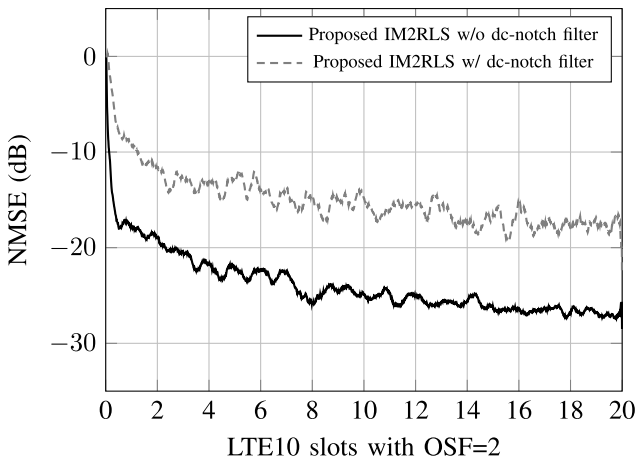

Fig. 8. Convergence of the IM2RLS w/o and w/ dc-notch filter for an LTE transmit signal with 10 MHz bandwidth, OSF of 2, and $P_{\mathrm{Tx}} = 23$ dBm. The wanted Rx signal power at the antenna input is $P_{\mathrm{Rx}} = -97$ dBm and the Rx SNR = 3 dB. The mixer IIP2 is +50 dBm, which corresponds to an Rx SNR desense of 4.4 dB.

TABLE I

IIP2 IMPROVEMENT BY DIGITAL CANCELLATION

IM2RLS Algorithm	$P_{\mathrm{IMD2}}^{\mathrm{CSF}}$ before	$P_{\mathrm{IMD2}}^{\mathrm{CSF}}$ after	IIP2 after canc.
w/o dc cancellation	-77.5 dBm	-95.8 dBm	68.4 dBm
w/ dc cancellation	-77.5 dBm	-94.5 dBm	67 dBm

50 dBm. This results in a desensitization of the wanted Rx signal from an SNR = 3 dB to an SINR of −1.4 dB at $P_{\mathrm{Tx}} = 23$ dBm. The I-path IMD2 interference is estimated by the IM2RLS using 15 taps, running at the sampling frequency of 30.72 MHz (OSF = 2). This means that the adaptive filter has less taps than the duplexer stopband impulse response which has 30 complex-valued coefficients at OSF = 2. The Q-path IMD2 replica is estimated by a linear 1-tap RLS (running at 30.72 MHz sampling rate), which uses the I-path IMD2 replica as a reference input.

The IM2RLS algorithm uses the forgetting factor $\lambda = 0.9999$ and $\mathbf{P}[-1] = 100\mathbf{I}$ as suggested in [37]. The 1-tap RLS in the Q-path uses the same forgetting factor and the initial coefficient $p[-1] = 10^7$. The coefficient vector of the I-path IM2RLS algorithm is initialized with $\mathbf{w}_{\mathrm{I}}[-1] = [10^{-6}, 0, 0, \ldots, 0]^{\mathrm{T}}$, and the 1-tap RLS with zero. Fig. 7 shows the steady-state SINR improvement at different transmit power levels for an IIP2 of +50 dBm. It can be observed that in both cases (w/o and w/ dc cancellation), the SINR is improved nearly up to the Rx SNR of 3 dB. The convergence behavior at the transmit power of 23 dBm is depicted in Fig. 8. For the hypothetical case that the receiver and the IM2RLS are using no dc suppression, the IM2RLS converges faster than with dc suppression. This is reasoned in the additional dc-IMD2 power, which supports the algorithm to converge faster. The IIP2 improvement by the digital cancellation is summarized in Table I and may be calculated for the IM2RLS with dc-notch filter via

$$\begin{aligned}\mathrm{IIP2}_{\text{after canc.}} &= 2P_{\mathrm{RF}}^{\mathrm{TxL}} - P_{\text{IM2, after canc.}}^{\mathrm{CSF,LTE}} - \mathrm{CF} \\ &= 2 \cdot (23\,\mathrm{dBm} - 50\ \mathrm{dB} + 20\ \mathrm{dB}) \\ &\quad + 94.5\ \mathrm{dBm} - 13.4\ \mathrm{dB} = 67\ \mathrm{dBm}. \end{aligned} \tag{28}$$

The IIP2 is improved from +50 dBm to 68.4 dBm and 67 dBm by the digital cancellation with the IM2RLS w/o and w/dc suppression, respectively. The correction factor of 13.4 dB corrects the IMD2 power calculated with the 2-tone formula, to the channel-select, and dc-filtered in-band IMD2 power for the LTE10 full allocation case [8]. For the calculation of the IIP2 improvement, the IMD2 power without dc is used in both cases. The derived IM2RLS algorithm with included dc-notch filter shows an excellent cancellation performance for a full-allocated LTE10 transmit signal. However, to improve numerical stability for small bandwidth allocations like, e.g., used in multi-cluster transmissions, the regularized IM2RLS (R-IM2RLS) is derived in the next section.

V. TIKHONOV REGULARIZATION OF THE NONLINEAR RLS

To reduce the spectral OOB emission of the LTE signals, not all available subcarriers are allocated. A portion of the subcarriers at the band-edges (guard-band) are forced to zero which introduces correlation in the transmit BB samples. For example, in a 10 MHz LTE signal, a maximum of 600 out of 1024 subcarriers may be occupied by data [38]. This correlation in the Tx BB signal $x_{\mathrm{BB}}[n]$ leads to a badly conditioned autocorrelation matrix $\mathbf{R} = E\{\mathbf{x}_{\mathrm{BB}}[n]\mathbf{x}_{\mathrm{BB}}^{\mathrm{H}}[n]\}$ and, respectively, $\tilde{\mathbf{R}} = E\{\mathbf{z}_{\mathrm{f}}[n]\mathbf{z}_{\mathrm{f}}^{\mathrm{H}}[n]\}$. The condition number of the autocorrelation matrix is determined by the ratio between the maximum and minimum singular value of the matrix. Algorithms which need the estimation of the autocorrelation matrix or its inverse $\mathbf{P} = \mathbf{R}^{-1}$ to estimate the system coefficients either iteratively or in batch-mode, are sensitive to the condition number of $\mathbf{R}$ and may suffer from numerical instability if $\mathbf{R}$ is badly conditioned. Because of this reason, a regularized version of the IM2RLS algorithm (R-IM2RLS) is derived in this section.

A common method to overcome the problem of badly conditioned autocorrelation matrices is regularization [35]. Adding a positive definite matrix to the estimated autocorrelation matrix in each iteration of the RLS algorithm guarantees

that the regularized autocorrelation matrix $\tilde{\mathbf{R}}'$ stays positive definite and maintains, therefore, the necessary condition for convergence and existence of $\mathbf{P} = \tilde{\mathbf{R}}'^{-1}$ [39].

This method is commonly known as Tikhonov-regularization where a matrix $\mathbf{L}$ is used for the regularization [40]. By including a regularization term in the cost function (15), the new cost function

$$\begin{aligned} J'_{\mathrm{R}}[n] &= \sum_{i=0}^{n} \lambda^{n-i} \left[|e_{\mathrm{I}}[i]|^2 + \sigma \left\| \mathbf{L}\mathbf{w}_{\mathrm{I}}[n] \right\|_2^2 \right] \\ &= \sum_{i=0}^{n} \lambda^{n-i} \left[|e_{\mathrm{I}}[i]|^2 + \sigma\, \mathbf{w}_{\mathrm{I}}^{\mathrm{T}}[n] \mathbf{L}^{\mathrm{T}} \mathbf{L} \mathbf{w}_{\mathrm{I}}^{*}[n] \right] \end{aligned} \tag{29}$$

is defined where $e_{\mathrm{I}}[i] = d_{\mathrm{I}}[i] - \mathbf{z}^{\mathrm{T}}[i]\mathbf{w}_{\mathrm{I}}^{*}[n] * h_s[i]$. The regularization parameter $\sigma \geq 0$ is used to adjust the regularization amount, and the real-valued matrix $\mathbf{L}$ is typically chosen as $\mathbf{L} = \mathbf{I}$ (standard Tikhonov regularization), $\mathbf{L} = \mathrm{upperbidiag}(1, -1)$ (first-order derivative), or

$$\mathbf{L} = \begin{bmatrix} -2 & 1 & & & \\ 1 & -2 & 1 & & \\ & 1 & -2 & 1 & \\ & & \ddots & \ddots & \ddots \\ & & & 1 & -2 \end{bmatrix} \tag{30}$$

(second-order derivative) [40]. Using the Wirtinger calculus [30] to obtain the gradient of the cost function (29), and setting the gradient to zero results in

$$\underbrace{\left[\sum_{i=0}^{n} \lambda^{n-i} \left(\mathbf{z}_{\mathrm{f}}[i] \mathbf{z}_{\mathrm{f}}^{\mathrm{H}}[i] + \sigma \mathbf{L}^{\mathrm{T}} \mathbf{L} \right) \right]}_{\tilde{\mathbf{R}}'[n]} \mathbf{w}_{\mathrm{I}}[n] = \underbrace{\sum_{i=0}^{n} \lambda^{n-i} d_{\mathrm{I}}[i] \mathbf{z}_{\mathrm{f}}[i]}_{\tilde{\mathbf{r}}[n]}. \tag{31}$$

Reformulating the above-mentioned equation leads to $\mathbf{w}_{\mathrm{I}}[n] = \tilde{\mathbf{R}}'^{-1}[n]\tilde{\mathbf{r}}[n] = \mathbf{P}[n]\tilde{\mathbf{r}}[n]$, which is solved recursively using the RLS algorithm. By expressing the cross-correlation vector $\tilde{\mathbf{r}}[n]$ by its previous estimate $\tilde{\mathbf{r}}[n-1]$, a recursive estimation of the form

$$\tilde{\mathbf{r}}[n] = \lambda \tilde{\mathbf{r}}[n-1] + d_{\mathrm{I}}[n] \mathbf{z}_{\mathrm{f}}[n] \tag{32}$$

may be formulated. Similarly, a recursive estimation of the regularized autocorrelation matrix is obtained by

$$\begin{aligned} \tilde{\mathbf{R}}'[n] &= \lambda \sum_{i=0}^{n-1} \lambda^{n-i-1} \left(\mathbf{z}_{\mathrm{f}}[i] \mathbf{z}_{\mathrm{f}}^{\mathrm{H}}[i] + \sigma \mathbf{L}^{\mathrm{T}} \mathbf{L} \right) \\ &\quad + \mathbf{z}_{\mathrm{f}}[n] \mathbf{z}_{\mathrm{f}}^{\mathrm{H}}[n] + \sigma \mathbf{L}^{\mathrm{T}} \mathbf{L} \\ &= \lambda \tilde{\mathbf{R}}'[n-1] + \sigma \mathbf{L}^{\mathrm{T}} \mathbf{L} + \mathbf{z}_{\mathrm{f}}[n] \mathbf{z}_{\mathrm{f}}^{\mathrm{H}}[n]. \end{aligned} \tag{33}$$

Substituting $\Omega[n]^{-1} = \lambda \tilde{\mathbf{R}}'[n-1] + \sigma \mathbf{L}^{\mathrm{T}} \mathbf{L}$ into (33), the matrix $\mathbf{P}[n] = \tilde{\mathbf{R}}'^{-1}[n]$ becomes

$$\mathbf{P}[n] = \left[\Omega[n]^{-1} + \mathbf{z}_{\mathrm{f}}[n] \mathbf{z}_{\mathrm{f}}^{\mathrm{H}}[n] \right]^{-1}. \tag{34}$$

After applying the matrix inversion lemma

$$(\mathbf{A} + \mathbf{BCD})^{-1} = \mathbf{A}^{-1} - \mathbf{A}^{-1}\mathbf{B}(\mathbf{C}^{-1} + \mathbf{D}\mathbf{A}^{-1}\mathbf{B})^{-1}\mathbf{D}\mathbf{A}^{-1} \tag{35}$$

to avoid the matrix inversion, (34) may be formulated as

$$\mathbf{P}[n] = \Omega[n] - \mathbf{k}[n] \mathbf{z}_{\mathrm{f}}^{\mathrm{H}}[n] \Omega[n] \tag{36}$$

using the gain vector

$$\mathbf{k}[n] = \frac{\Omega[n] \mathbf{z}_{\mathrm{f}}[n]}{1 + \mathbf{z}_{\mathrm{f}}^{\mathrm{H}}[n] \Omega[n] \mathbf{z}_{\mathrm{f}}[n]}. \tag{37}$$

For the inversion

$$\Omega[n] = [\lambda \mathbf{P}^{-1}[n-1] + \sigma \mathbf{L}^{\mathrm{T}} \mathbf{L}]^{-1} \tag{38}$$

again the matrix inversion lemma is applied, which yields

$$\Omega[n] = \frac{1}{\lambda} (\mathbf{P}[n-1] - \Sigma[n] \mathbf{L} \mathbf{P}[n-1]) \tag{39}$$

where the substitution

$$\Sigma[n] = \sigma \mathbf{P}[n-1] \mathbf{L}^{\mathrm{T}} [\lambda \mathbf{I} + \sigma \mathbf{L} \mathbf{P}[n-1] \mathbf{L}^{\mathrm{T}}]^{-1} \tag{40}$$

is used. After rearranging (40), the expression

$$\Sigma[n] = \frac{\sigma}{\lambda} \left(\mathbf{P}[n-1] - \Sigma[n] \mathbf{L} \mathbf{P}[n-1] \right) \mathbf{L}^{\mathrm{T}} = \sigma \Omega[n] \mathbf{L}^{\mathrm{T}} \tag{41}$$

is obtained. Unfortunately, the calculation of $\Sigma[n]$ in (40), and therefore, $\Omega[n]$ still includes a matrix inversion after applying the matrix inversion lemma. However, by decomposing the matrix $\mathbf{L}^{\mathrm{T}}\mathbf{L}$ in (38) into a sum of V dyads [41]

$$\Omega[n] = \left[\lambda \mathbf{P}^{-1}[n-1] + \sigma \sum_{k=1}^{V} \mathbf{p}_{k,1} \mathbf{p}_{k,2}^{\mathrm{T}} \right]^{-1} \tag{42}$$

applying the matrix inversion lemma results in the recursive calculation of (42) via

$$\Omega_k[n] = \Omega_{k-1}[n] - \frac{\Omega_{k-1}[n] \mathbf{p}_{k,1}}{\frac{1}{\sigma} + \mathbf{p}_{k,2}^{\mathrm{T}} \Omega_{k-1}[n] \mathbf{p}_{k,1}} \mathbf{p}_{k,2}^{\mathrm{T}} \Omega_{k-1}[n] \tag{43}$$

for $k = 1 \ldots V$ in each iteration n and $\Omega_0[n] = (1/\lambda)\mathbf{P}[n-1]$. Reformulating (37) yields

$$\mathbf{k}[n] = \mathbf{P}[n] \mathbf{z}_{\mathrm{f}}[n]. \tag{44}$$

The recursive update of the coefficient vector $\mathbf{w}_{\mathrm{I}}[n]$ is obtained by inserting [32], [36], [39], [41], and [44] into $\mathbf{w}_{\mathrm{I}}[n] = \mathbf{P}[n]\tilde{\mathbf{r}}[n]$. The final nonlinear R-IM2RLS algorithm to estimate the I-path IMD2 interference is summarized by:

$$\hat{y}_{\mathrm{I}}[n] = \mathbf{z}^{\mathrm{T}}[n] \mathbf{w}_{\mathrm{I}}^{*}[n-1] * h_s[n] \tag{45}$$

$$e_{\mathrm{I}}[n] = d_{\mathrm{I}}[n] - \hat{y}_{\mathrm{I}}[n] \tag{46}$$

$$\Omega_k[n] = \Omega_{k-1}[n] - \frac{\Omega_{k-1}[n] \mathbf{p}_{k,1}}{\frac{1}{\sigma} + \mathbf{p}_{k,2}^{\mathrm{T}} \Omega_{k-1}[n] \mathbf{p}_{k,1}} \mathbf{p}_{k,2}^{\mathrm{T}} \Omega_{k-1}[n] \tag{47}$$

$$\mathbf{k}[n] = \frac{\Omega_V[n] \mathbf{z}_{\mathrm{f}}[n]}{1 + \mathbf{z}_{\mathrm{f}}^{\mathrm{H}}[n] \Omega_V[n] \mathbf{z}_{\mathrm{f}}[n]} \tag{48}$$

$$\mathbf{P}[n] = \Omega_V[n] - \mathbf{k}[n] \mathbf{z}_{\mathrm{f}}^{\mathrm{H}}[n] \Omega_V[n] \tag{49}$$

$$\Sigma[n] = \sigma \Omega_V[n] \mathbf{L}^{\mathrm{T}} \tag{50}$$

$$\mathbf{w}_{\mathrm{I}}[n] = \left[\mathbf{I} - \left(\mathbf{I} - \mathbf{k}[n] \mathbf{z}_{\mathrm{f}}^{\mathrm{H}}[n] \right) \Sigma[n] \mathbf{L} \right] \mathbf{w}_{\mathrm{I}}[n-1] + \mathbf{k}[n] e_{\mathrm{I}}[n] \tag{51}$$

The proposed algorithm is initialized with $\mathbf{w}_{\mathrm{I}}[-1] \neq \mathbf{0}$, $0 \ll \lambda \leq 1$ and $\mathbf{P}[-1] = \nu\,\mathbf{I}$ with $\nu > 0$. When the dc suppression is used, then the R-IM2RLS update equations become:

$$\hat{y}_{\mathrm{I}}[n] = \mathbf{z}^{\mathrm{T}}[n]\mathbf{w}_{\mathrm{I}}^{*}[n-1] * h_s[n] \tag{52}$$

$$\hat{y}_{\mathrm{ac,I}}[n] = 0.998\,\hat{y}_{\mathrm{ac,I}}[n-1] + \hat{y}_{\mathrm{I}}[n] - \hat{y}_{\mathrm{I}}[n-1] \tag{53}$$

$$e_{\mathrm{ac,I}}[n] = d_{\mathrm{ac,I}}[n] - \hat{y}_{\mathrm{ac,I}}[n] \tag{54}$$

$$\Omega_k[n] = \Omega_{k-1}[n] - \frac{\Omega_{k-1}[n]\mathbf{p}_{k,1}}{\frac{1}{\sigma} + \mathbf{p}_{k,2}^{\mathrm{T}}\Omega_{k-1}[n]\mathbf{p}_{k,1}}\mathbf{p}_{k,2}^{\mathrm{T}}\Omega_{k-1}[n] \tag{55}$$

$$\mathbf{k}[n] = \frac{\Omega_V[n]\mathbf{z}_{\mathrm{f}}[n]}{1 + \mathbf{z}_{\mathrm{f}}^{\mathrm{H}}[n]\Omega_V[n]\mathbf{z}_{\mathrm{f}}[n]} \tag{56}$$

$$\mathbf{P}[n] = \Omega_V[n] - \mathbf{k}[n]\mathbf{z}_{\mathrm{f}}^{\mathrm{H}}[n]\Omega_V[n] \tag{57}$$

$$\Sigma[n] = \sigma\,\Omega_V[n]\mathbf{L}^{\mathrm{T}} \tag{58}$$

$$\mathbf{w}_{\mathrm{I}}[n] = \left[\mathbf{I} - \left(\mathbf{I} - \mathbf{k}[n]\mathbf{z}_{\mathrm{f}}^{\mathrm{H}}[n]\right)\Sigma[n]\mathbf{L}\right]\mathbf{w}_{\mathrm{I}}[n-1] + \mathbf{k}[n]e_{\mathrm{ac,I}}[n]. \tag{59}$$

The dc-notch filter (53) is used to remove the dc from the IMD2 replica (52). The complexity of the R-IM2RLS with dc-notch filter and $\mathbf{L} = \mathbf{I}$ is 8 $N_{\mathbf{w}}^3 + 21N_{\mathbf{w}}^2 + 5N_{\mathrm{CSF}} + 18N_{\mathbf{w}} + 1$ real multiplications and 2 $N_{\mathbf{w}}^2 + 2N_{\mathbf{w}}$ real divisions per iteration.

VI. Simulation Environment

The performance of the R-IM2RLS algorithm with the three above-mentioned regularization matrices $\mathbf{L}$ is evaluated with a FDD scenario using a LTE10 multi-cluster intra-band Tx signal, which has a native sampling frequency of $f_s = 15.36$ MHz, QPSK modulation and short cyclic prefix. The IMD2 interference in the I-path is estimated by the R-IM2RLS, while the Q-path IMD2 is estimated by a linear 1-tap RLS which uses the I-path IMD2 replica as a reference input. The resulting multi-cluster TxL signal has a strong frequency-selectivity like indicated in Fig. 9. The R-IM2RLS in the I-path has 15 taps and runs on the higher sampling rate of 30.72 MHz due to the OSF of 2. This means that the adaptive filter has fewer taps than the impulse response which is estimated. The linear 1-tap Q-path RLS runs also on the sampling rate of 30.72 MHz. The received signal $d[n]$ is dc filtered and the proposed algorithm is using the dc-notch filter to suppress the dc of the IMD2 replica signal. The wanted Rx signal has a power of $P_{\mathrm{Rx}} = -97$ dBm at the antenna with an SNR of 3 dB. The assumed Rx mixer IIP2 is +60 dBm, which corresponds to an Rx SNR desense of 1 dB for the specific intra-band multi-cluster transmit signal at 23 dBm power level. The thermal noise floor of the receiver is assumed at −104.5 dBm per 10 MHz and the receiver NF is 4.5 dB. The resulting receiver noise floor and Rx power with 20 dB LNA gain are at −80 dBm $\widehat{=}$ −108.2 dBm/15 kHz and −77 dBm, respectively. The spectrum of the signals at $P_{\mathrm{Tx}} = 23$ dBm is depicted in Fig. 9. It can be observed that the resulting IMD2 interference $y_{\mathrm{BB}}^{\mathrm{IMD2}}$ is mostly below the receiver noise floor but still leads to an SNR degradation of 1 dB. The estimated interference replica $\hat{y}_{\mathrm{ac}}[n] = \hat{y}_{\mathrm{ac,I}}[n] + j\hat{y}_{\mathrm{ac,Q}}[n]$ closely matches the true IMD2 interference $y_{\mathrm{BB}}^{\mathrm{IMD2}}$. The R-IM2RLS algorithm in the I-path uses the regularization parameters

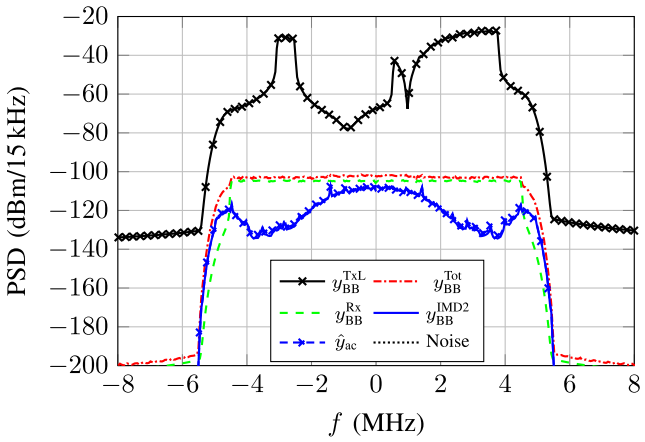

Fig. 9. Equivalent BB spectrum of the frequency-selective Tx leakage signal $y_{\mathrm{BB}}^{\mathrm{TxL}}$ (the corresponding passband signal is located at f_{Tx}) and the total received signal $y_{\mathrm{BB}}^{\mathrm{Tot}}$ after amplification with 20 dB LNA gain. The wanted Rx signal with SNR = 3 dB, and the receiver noise floor after amplification with 20 dB LNA gain are at −77 dBm and −80 dBm $\widehat{=}$ −108.2 dBm/15 kHz respectively. The total received signal contains the dc-filtered, and channel-select filtered IMD2 interference at $P_{\mathrm{Tx}} = 23$ dBm, and the IIP2 is 60 dBm.

$\sigma = 3 \times 10^{-7}$ and $\mathbf{L} = \mathbf{I}$. The multi-cluster LTE10 Tx signal uses 21/50 RBs (252 subcarriers from 1024), which means that 3.78 MHz of the available 9.015 MHz are allocated. With an OSF of 2, this corresponds to an allocated bandwidth-to-sampling-rate ratio of 3.78/30.72 = 0.12, which introduces a high correlation in the transmit BB samples. The resulting condition number cond($\tilde{\mathbf{R}}$) of the 15×15 dimensional autocorrelation matrix $\tilde{\mathbf{R}} = E\{\mathbf{z}_{\mathrm{f}}\mathbf{z}_{\mathrm{f}}^{\mathrm{H}}\}$ is in the order of 10^7, which results in a bad conditioned estimation, and may lead to numerical problems. The regularization of the R-IM2RLS improves numerical estimation of the matrix $\mathbf{P}[n]$ by lowering the condition number of the regularized matrix $\tilde{\mathbf{R}}'$.

A. IMD2 Self-Interference of a Multi-Cluster Tx Signal

For the estimation of the resulting IMD2 interference bandwidth, the bandwidth between the minimum and maximum allocated subcarrier in the multi-cluster Tx signal is of interest. In the used clustered LTE10 transmit signal, the allocated RBs are $\{9-11, 29-46\}$ with a numbering from left to right and the total number of 50 RBs. For the IMD2 bandwidth estimation, the resulting bandwidth between the lowest allocated subcarrier (RB 9) and the upper edge (RB 46) of the allocated RBs is $(3 + 17 + 18) \cdot 12 \cdot 15$ kHz = 6.84 MHz. Each RB has 12 subcarriers and 15 kHz subcarrier spacing. The resulting IMD2 interference bandwidth is 2×6.84 MHz = 13.68 MHz, which means that a small portion of the IMD2 interference is suppressed by the CSF. The full IMD2 interference including the dc, the IMD2 interference after the CSF and dc-removal, and the estimated IMD2 replica is visualized in Fig. 10. It can be observed that the R-IM2RLS is able to estimate the IMD2 interference down to 20 dB below the receiver noise floor.

B. Numerical Simulation Results

In the following simulation results, the IMD2 self-interference cancellation performance in case of an

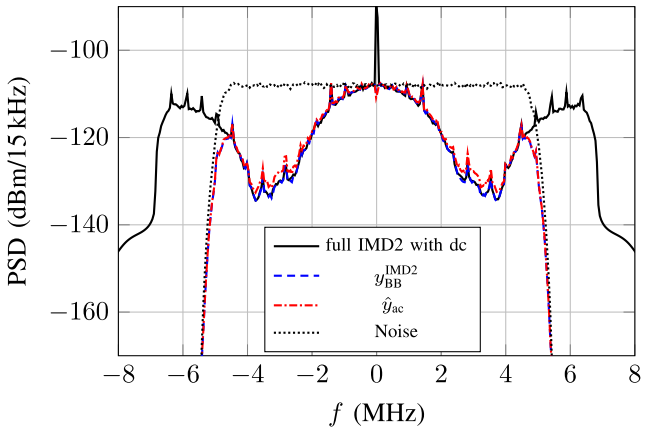

Fig. 10. Generated IMD2 interference with the bandwidth of 13.68 MHz at $P_{Tx} = 23$ dBm. The resulting in-band BB IMD2 interference y_{BB}^{IMD2} after the CSF and dc-removal is below the receiver noise floor. The R-IM2RLS estimates the IMD2 interference down to 20 dB below the noise floor.

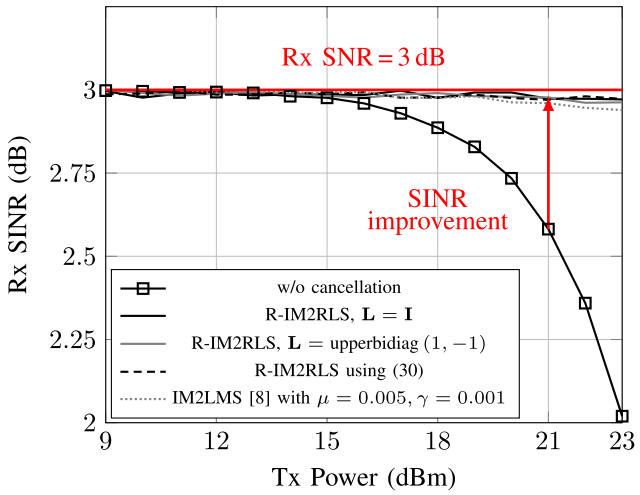

Fig. 11. Improvement of the Rx SINR at different transmitter power levels and an Rx mixer IIP2 of +60 dBm. The algorithms are using the dc-filtered receive signal, and the R-IM2RLS/IM2LMS algorithms are using the dc-notch filter to remove the dc. The wanted signal at the antenna has the power $P_{Rx} = -97$ dBm and an SNR of 3 dB.

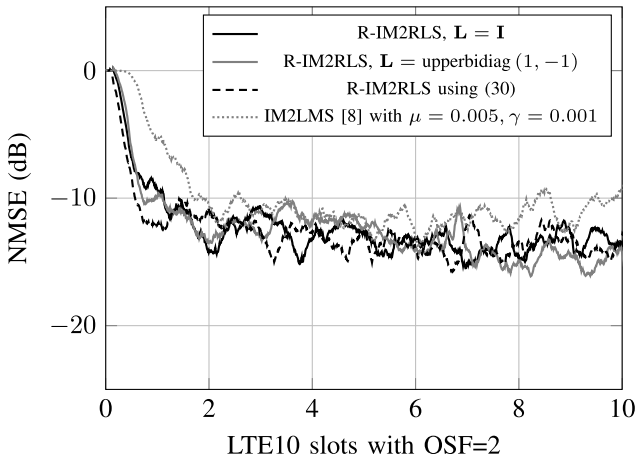

Fig. 12. Convergence of the R-IM2RLS with different regularization matrices and the IM2LMS algorithm at the transmit power level of $P_{Tx} = 23$ dBm. The algorithms are using the dc-notch filter to suppress the dc.

intra-band multi-cluster Tx signal, using the R-IM2RLS algorithm (52)–(59) and using the dc-notch filter with different regularization matrices is evaluated. The forgetting factor of the R-IM2RLS is chosen as $\lambda = 0.9999$, $\mathbf{P}[-1] = 100\mathbf{I}$, and the regularization constant $\sigma = 3 \times 10^{-7}$. The 1-tap RLS in the Q-path uses the same forgetting factor but the initial coefficient $p[-1] = 10^7$. The coefficient vector of the R-IM2RLS is initialized with $\mathbf{w}_I[-1] = [10^{-6}, 0, 0, \ldots, 0]^T$ for the I-path, and the 1-tap Q-path RLS is initialized with zero. The performance is evaluated for different regularization matrices $\mathbf{L} = \mathbf{I}$ (Tikhonov regularization), $\mathbf{L} = \text{upperbidiag}(1, -1)$ (first-order derivative smoothing matrix), and $\mathbf{L} = \text{diag}(1, -2, 1)$ (second-order derivative smoothing matrix). The IM2RLS without regularization is not included in the comparison due to numerical instability reasoned by the extremely high condition number of $\tilde{\mathbf{R}}$ which is in the order of 10^7. The performance of the R-IM2RLS is compared with the recently published LMS-type algorithm (IM2LMS) [8]. The IM2LMS uses the step-size $\mu = 0.005$, the regularization parameter $\gamma = 0.001$, and the initial coefficient vector $\mathbf{w}_I[-1] = [10^{-4}, 0, 0, \ldots, 0]^T$. The Q-path IMD2 replica is estimated by a linear normalized 1-tap LMS, which uses the I-path IMD2 replica estimated by the IM2LMS as a reference input. The normalized 1-tap LMS uses a step-size of 1, the regularization parameter is set to 10^{-7}, and the initial coefficient is set to zero. The value of the step-size is set to the best compromise between steady-state cancellation and convergence time. The convergence of the algorithms is compared using the ensemble normalized mean-square-error (NMSE), and the steady-state cancellation by the SINR. The SINR improvement of the Rx signal for different algorithms and regularizations is depicted in Fig. 11. The regularization improves the stability of the algorithm, but on the other hand, it also reduces the estimation accuracy. Consequently, the regularization is a tradeoff between stability and accuracy. The convergence behavior of the algorithms is depicted in Fig. 12. The R-IM2RLS shows a faster initial convergence than the IM2LMS algorithm which takes about twice as long to reach an NMSE of −10 dB. The evolution of the condition number of $\tilde{\mathbf{R}}'[n] = \mathbf{P}[n]^{-1}$ is illustrated in Fig. 13. The condition number of $\tilde{\mathbf{R}}$ estimated by the IM2RLS without regularization drastically increases up to values between 10^7 and 10^8. In contrast to that, the condition number of $\tilde{\mathbf{R}}'$ estimated by the R-IM2RLS with different regularization matrices $\mathbf{L}$ stays below 400 for the specific clustered Tx example. The achieved IIP2 after the digital IMD2 cancellation is summarized in Table II. The R-IM2RLS and IM2LMS algorithms are improving the IIP2 from 60 dBm to about 77 dBm and 73 dBm, respectively.

VII. Verification of the Derived Algorithm With Measurement Data

The proposed R-IM2RLS algorithm is evaluated with measurement data and MATLAB post-processing. The measurement setup (A) depicted in Fig. 14 includes the nonlinear PA

TABLE II

IIP2 IMPROVEMENT BY DIGITAL CANCELLATION FOR THE CLUSTERED TX SIGNAL

Algorithm	IIP2 after canc.
R-IM2RLS, $\mathbf{L} = \mathbf{I}$	77.2 dBm
R-IM2RLS, $\mathbf{L}$ = upperbidiag $(1, -1)$	76.5 dBm
R-IM2RLS using (30)	76.4 dBm
IM2LMS [8]	73 dBm

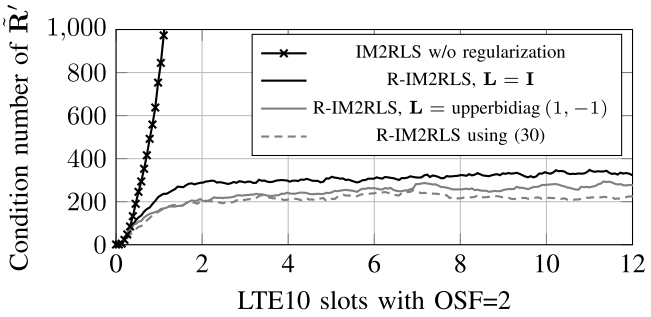

Fig. 13. Evolution of the condition number of $\tilde{\mathbf{R}}'[n] = \mathbf{P}^{-1}[n]$ for a clustered allocation like depicted in Fig. 9 and 23 dBm transmit power. The condition number of $\tilde{\mathbf{R}} = E\{\mathbf{z}\mathbf{z}^{\mathrm{H}}\}$ without regularization is in the order of 10^7 to 10^8.

ZVA-183G+, which has a gain of 38 dB, a 1 dB compression point of $P_{1\mathrm{dB}} = 25$ dBm, and an IP3 of 36 dBm. The output of the PA is connected to the commercial LTE band 2 duplexer model B8663 from TDK. The antenna port of the duplexer is terminated with a 50 Ω impedance, and the Rx port of the duplexer is connected to the LNA ZX60-83LN12+ which has 22 dB gain, a NF of 1.4 dB, and an IP3 of 35.2 dBm (at 2 GHz). For the downconversion, the ZAM-42 Level 7 mixer is used, which has 25 dB LO-to-RF terminal isolation. No additional filters are used in the transmitter and receiver chain. The measurement is carried out for the I-path mixer and a full-allocated LTE-A transmit signal with 10 MHz bandwidth, QPSK modulation, and short cyclic prefix. The transmit frequency is set to $f_{\mathrm{Tx}} = 1.855$ GHz and the mixer LO frequency is $f_{\mathrm{Rx}} = 1.935$ GHz (80 MHz duplexing distance). The LTE transmit signal is generated with the R&S SMW 200A signal generator (B) and amplified by the PA. The transmit signal leaks through the duplexer stopband into the receiver with 80 MHz frequency offset to the LO signal and is amplified by the LNA. This amplified TxL signal generates the BB IMD2 interference at the output of the mixer which is measured with the real-time oscilloscope RTO 1044 (C) using the BB I/Q-interface (RTO-K11 option). This option allows to set the oscilloscope sampling frequency to the native LTE sampling frequency (a sampling rate of 15.36 MHz for 10 MHz LTE signals is used) and also includes a channel-select filtering. The TxL signal at the output of the LNA is measured by the R&S FSW26 spectrum analyzer (D), and the LO signal with 7 dBm for the ZAM-42 mixer is generated by the R&S SMB 100A signal generator (E). The measurement of the TxL signal and the BB IMD2 interference are performed consecutively such that the circuit load is always kept constant with 50 Ω impedance. The transmit power at the output of the PA is set to $P_{\mathrm{RF}}^{\mathrm{Tx}} = 24$ dBm, which in combination with

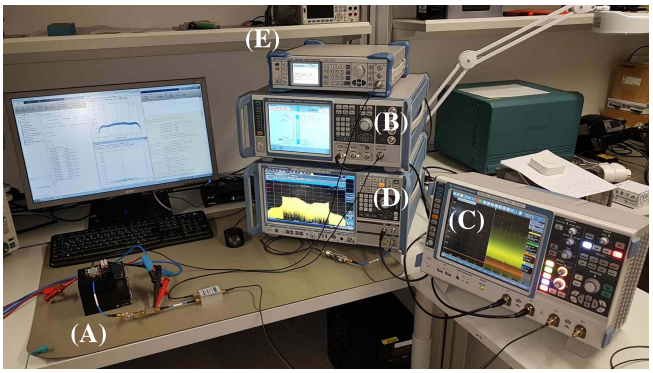

Fig. 14. Measurement setup including the DUT (A) with the PA ZVA-183G+, the LNA ZX60-83LN12+, the mixer ZAM-42 from Mini Circuits, and the LTE band 2 duplexer B8663. The signal generator R&S SMW 200A (B) generates the LTE transmit signal which is amplified by the PA. The R&S real-time oscilloscope RTO 1044 (C) is used to measure the BB signal at the output of the mixer. The R&S FSW26 spectrum analyzer (D) is used to measure the TxL signal, and the signal generator R&S SMB 100A (E) generates the mixer LO signal.

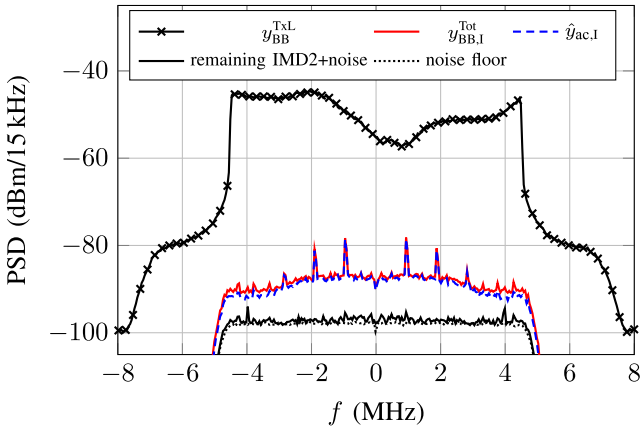

Fig. 15. Spectrum of the measured BB equivalent TxL signal $y_{\mathrm{BB}}^{\mathrm{TxL}}$ and the receive signal $y_{\mathrm{BB,I}}^{\mathrm{Tot}}$ including noise and the IMD2 interference. The BB equivalent TxL signal shows a strong frequency selectivity. Also shown are the spectrum of the estimated IMD2 replica $\hat{y}_{\mathrm{ac,I}}$ and the remaining IMD2 and noise after the cancellation.

the duplexer attenuation of 66.6 dB (at $f_{\mathrm{Tx}} = 1.855$ GHz) and the LNA gain of 22 dB leads to the TxL signal power of $P_{\mathrm{RF}}^{\mathrm{TxL}} = 24$ dBm $-$ 66.6 dB $+$ 22 dB $= -20.6$ dBm. The measured I-path mixer BB output data stream and the complex-valued BB transmit samples are up-sampled by the factor of 2 (because the proposed algorithm includes the envelope-squaring which doubles the signal bandwidth) and used for the MATLAB post-processing. The spectrum of the signals before and after digital cancellation with the R-IM2RLS using a Tikhonov regularization, and the parameters $\mathbf{P}[-1] = 1000\mathbf{I}$, $\lambda = 0.99999$, $\sigma = 10^{-6}$, and $\mathbf{L} = \mathbf{I}$ are depicted in Fig. 15. The MATLAB post-cancellation showed that 15 taps were sufficient to reduce the received signal power by 9.3 dBm nearly down to the noise floor. The coefficient vector was initialized with $\mathbf{w}_{\mathrm{I}}[-1] = [10^{-6}, 0, 0, \ldots, 0]^{\mathrm{T}}$, and the convergence behavior of the 15 coefficients is shown in Fig. 16, which indicates that the algorithm converged after about five LTE symbols.

To determine the IIP2 improvement by the digital cancellation, the true BB IMD2 interference signal needs to be known.

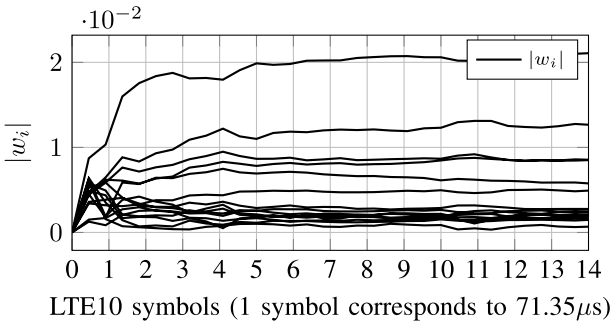

Fig. 16. Evolution of the 15 coefficients w_i for $i = 0 \ldots 14$ which are estimated by the R-IM2RLS algorithm. Plotted are the absolute values of the complex-valued coefficients. Convergence is achieved after around five LTE symbols (one LTE symbol has the duration of 71.35μs).

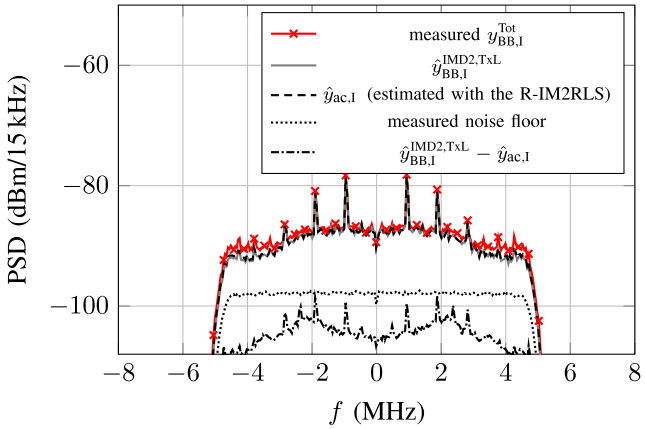

Fig. 17. Spectrum of the reconstructed IMD2 signal $\hat{y}_{\mathrm{BB,I}}^{\mathrm{IMD2,TxL}}$ using the measured TxL signal. The IMD2 signal which is estimated by the R-IM2RLS algorithm using the total received signal $y_{\mathrm{BB,I}}^{\mathrm{Tot}}$ and the ideal transmit IQ-samples closely matches the reconstructed IMD2 signal. The remaining IMD2 signal spectrum lies below the noise floor.

In the measurement, the true IMD2 interference is embedded in noise and cannot be measured explicitly. In addition, the correction factor used in (28) is not known. However, the true IMD2 signal may be approximately reconstructed by computing the envelope of the measured TxL signal

$$\hat{y}_{\mathrm{BB,I}}^{\mathrm{IMD2,TxL}}[n] = \alpha_2^{\mathrm{TxL,I}} \left| y_{\mathrm{BB}}^{\mathrm{TxL}}[n] \right|^2 * \bar{h}_s[n] \tag{60}$$

with subsequent channel-select filtering and removal of the dc component. Finally, the factor $\alpha_2^{\mathrm{TxL,I}}$ is adjusted till the reconstructed IMD2 interference $\hat{y}_{\mathrm{BB,I}}^{\mathrm{IMD2,TxL}}$ matches as good as possible the spectrum of the measured signal $y_{\mathrm{BB,I}}^{\mathrm{Tot}}$. The resulting spectrum of the reconstructed IMD2 interference using (60) is depicted in Fig. 17 and it can be observed that a good match with the total received signal $y_{\mathrm{BB}}^{\mathrm{Tot,I}}$ is achieved. Also, the error signal between the reconstructed IMD2 interference $\hat{y}_{\mathrm{BB,I}}^{\mathrm{IMD2,TxL}}$ and the IMD2 replica signal obtained by the R-IM2RLS algorithm is visualized. Finally, the obtained IMD2 cancellation is estimated by using the NMSE in steady state [6] using

$$\begin{aligned} \mathrm{NMSE_{dB}} &= 10 \log_{10} \left(\frac{\mathrm{E}\left[\left| \hat{y}_{\mathrm{BB,I}}^{\mathrm{IMD2,TxL}}[n] - \hat{y}_{\mathrm{ac,I}}[n] \right|^2 \right]}{\mathrm{E}\left[\left| \hat{y}_{\mathrm{BB,I}}^{\mathrm{IMD2,TxL}}[n] \right|^2 \right]} \right) \\ &= -16 \text{ dB} \end{aligned} \tag{61}$$

which indicates an IMD2 interference cancellation of 16 dB. On the other hand, this corresponds to an increase of the IIP2 of the same amount.

The provided measurement results indicate that in spite of the in-band distortions caused by the PA, the ideal Tx IQ-samples can be used as an input signal to the cancellation algorithm. The same should be true in a chip implementation, where a lot of effort is spent to keep the overall architecture dependent in-band distortions as small as possible [42].

VIII. Conclusion

In this paper, we developed a novel nonlinear RLS-type adaptive filter (IM2RLS) and its robust version (R-IM2RLS) for the digital IMD2 self-interference cancellation in LTE FDD direct conversion RF transceivers. The R-IM2RLS provides stability and numerical tractability for highly correlated transmit signals which may result in an ill-conditioned autocorrelation matrix. The proposed R-IM2RLS algorithm was able to cancel the IMD2 interference, which was generated by a Tx leakage signal that traveled through a highly frequency-selective duplexer stopband. Its performance was evaluated with different regularization matrices. Typical RF receivers use a dc cancellation to prevent the ADC from saturation and a CSF to limit the signal bandwidth. Therefore, the IMD2 interference which is generated by the second-order nonlinearity in the mixer is dc filtered and its bandwidth is reduced to the LTE signal bandwidth. Consequently, the adaptive filter needs to provide a dc-filtered in-band IMD2 replica. This contribution showed that the IM2RLS/R-IM2RLS adaptive filter is able to reproduce the in-band IMD2 interference without dc by including the CSF and a dc-notch filter within the algorithm. Depending on the initialization of the coefficient vector, we observed that the proposed algorithm may adapt to different solutions of the coefficient vector. However, due to the envelope-squaring within the proposed IM2RLS algorithm, the correct IMD2 replica signal is reconstructed. For the multi-cluster transmit signal which was used in our simulation, the algorithm converged within one LTE slot (seven LTE symbols), and the steady-state Rx SNR degradation by the IMD2 self-interference was improved from 1 dB to less than 0.05 dB. The performance of the R-IM2RLS was assessed in a LTE measurement scenario with discrete RF components. With the measured TxL signal, a IMD2 reference signal was reconstructed which allowed the estimation of the IIP2 improvement. The IMD2 interference in the received signal was suppressed by 16 dB and an adaptation of the estimated coefficients within five LTE symbols (357 μs) was achieved.

Acknowledgment

The authors would like to thank DMCE GmbH & Co KG, Linz, Austria, as part of Intel for supporting this paper carried out at the Christian Doppler Laboratory for Digitally Assisted RF Transceivers for Future Mobile Communications, Linz.

References

[1] *REFSENS With One UL Carrier for NC Intra-Band CA*, document R4-126964, Ericsson and ST-Ericsson, Nov. 2012. [Online]. Available: http://www.3gpp.org/ftp/tsg_ran/WG4_Radio/TSGR4_65/docs/R4-126964.zip

[2] R. Vazny, W. Schelmbauer, H. Pretl, S. Herzinger, and R. Weigel, "An interstage filter-free mobile radio receiver with integrated TX leakage filtering," in *Proc. IEEE Radio Freq. Integr. Circuits Symp. (RFIC)*, May 2010, pp. 21–24.

[3] C. W. Liu and M. Damgaard, "IP2 and IP3 nonlinearity specifications for 3G/WCDMA receivers," in *Proc. High Freq. Electron.*, 2009, pp. 16–29.

[4] A. Kiayani, L. Anttila, M. Kosunen, K. Stadius, J. Ryynänen, and M. Valkama, "Modeling and joint mitigation of Tx and RX nonlinearity-induced receiver desensitization," *IEEE Trans. Microw. Theory Techn.*, vol. 65, no. 7, pp. 2427–2442, Jul. 2017.

[5] A. Kiayani, M. Abdelaziz, L. Anttila, V. Lehtinen, and M. Valkama, "Digital mitigation of transmitter-induced receiver desensitization in carrier aggregation FDD transceivers," *IEEE Trans. Microw. Theory Techn.*, vol. 63, no. 11, pp. 3608–3623, Nov. 2015.

[6] A. Gebhard, R. Kanumalli, B. Neurauter, and M. Huemer, "Adaptive self-interference cancelation in LTE-A carrier aggregation FDD direct-conversion transceivers," in *Proc. 9th IEEE Sensor Array Multichannel Signal Process. Conf. (SAM)*, Jul. 2016, pp. 1–5.

[7] A. Kiayani, L. Anttila, and M. Valkama, "Modeling and dynamic cancellation of TX-RX leakage in FDD transceivers," in *Proc. IEEE 56th Int. Midwest Symp. Circuits Syst. (MWSCAS)*, Aug. 2013, pp. 1089–1094.

[8] A. Gebhard, C. Motz, R. Kanumalli, H. Pretl, and M. Huemer, "Nonlinear least-mean-squares type algorithm for second-order interference cancellation in LTE-A RF transceivers," in *Proc. 51st Asilomar Conf. Signals, Syst., Comput.*, Oct. 2017, pp. 802–807.

[9] A. Kiayani *et al.*, "Adaptive nonlinear RF cancellation for improved isolation in simultaneous transmit–receive systems," *IEEE Trans. Microw. Theory Tech.*, vol. 66, no. 5, pp. 2299–2312, May 2018.

[10] H. Khatri, P. S. Gudem, and L. E. Larson, "An active transmitter leakage suppression technique for CMOS SAW-Less CDMA receivers," *IEEE J. Solid-State Circuits*, vol. 45, no. 8, pp. 1590–1601, Aug. 2010.

[11] A. Elmaghraby *et al.*, "A mixed-signal technique for TX-induced modulated spur cancellation in LTE-CA receivers," *IEEE Trans. Circuits Syst. I, Reg. Papers*, vol. 65, no. 9, pp. 3060–3073, Sep. 2018.

[12] R. Kanumalli, A. Gebhard, A. Elmaghraby, A. Mayer, D. Schwarty, and M. Huemer, "Active digital cancellation of transmitter induced modulated spur interference in 4G LTE carrier aggregation transceivers," in *Proc. 83rd Veh. Technol. Conf. (VTC Spring)*, May 2016, pp. 1–5.

[13] S. Sadjina, R. S. Kanumalli, A. Gebhard, K. Dufrêne, M. Huemer, and H. Pretl, "A mixed-signal circuit technique for cancellation of interferers modulated by LO phase-noise in 4G/5G CA transceivers," *IEEE Trans. Circuits Syst. I, Reg. Papers*, vol. 65, no. 11, pp. 3745–3755, Nov. 2018.

[14] A. Kiayani, L. Anttila, and M. Valkama, "Digital suppression of power amplifier spurious emissions at receiver band in FDD transceivers," *IEEE Signal Process. Lett.*, vol. 21, no. 1, pp. 69–73, Jan. 2014.

[15] B. Razavi, "Design considerations for direct-conversion receivers," *IEEE Trans. Circuits Syst. II, Analog Digit. Signal Process.*, vol. 44, no. 6, pp. 428–435, Jun. 1997.

[16] C. Lederer and M. Huemer, "LMS based digital cancellation of second-order TX intermodulation products in homodyne receivers," in *Proc. IEEE Radio Wireless Symp. (RWS)*, Jan. 2011, pp. 207–210.

[17] A. Frotzscher and G. Fettweis, "A stochastic gradient LMS algorithm for digital compensation of Tx leakage in zero-IF-receivers," in *Proc. Veh. Technol. Conf. (VTC Spring)*, May 2008, pp. 1067–1071.

[18] M. Kahrizi, J. Komaili, J. E. Vasa, and D. Agahi, "Adaptive filtering using LMS for digital TX IM2 cancellation in WCDMA receiver," in *Proc. IEEE Radio Wireless Symp.*, Jan. 2008, pp. 519–522.

[19] A. Frotzscher and G. Fettweis, "Least squares estimation for the digital compensation of Tx leakage in zero-IF receivers," in *Proc. Global Telecommun. Conf. (GLOBECOM)*, Nov. 2009, pp. 1–6.

[20] H. Gheidi, H.-T. Dabag, Y. Liu, P. M. Asbeck, and P. Gudem, "Digital cancellation technique to mitigate receiver desensitization in cellular handsets operating in carrier aggregation mode with multiple uplinks and multiple downlinks," in *Proc. IEEE Radio Wireless Symp.*, Jan. 2015, pp. 221–224.

[21] V. J. Mathews and G. L. Sicuranza, *Polynomial Signal Processing*, vol. 27. Hoboken, NJ, USA: Wiley, 2000.

[22] C. Lederer and M. Huemer, "Simplified complex LMS algorithm for the cancellation of second-order TX intermodulation distortions in homodyne receivers," in Proc. *Proc. 45th Asilomar Conf. Signals, Syst. Comput. (ASILOMAR)*, Nov. 2011, pp. 533–537.

[23] A. Walid, "Effective IM2 products estimation for two-tone and W-CDMA modulated blockers in 3GPP direct-conversion receivers," Maxim Integr., San Jose, CA, USA, Appl. Note 3380, Oct. 2004. [Online]. Available: https://pdfserv.maximintegrated.com/en/an/AN3380.pdf

[24] E. S. Atalla, A. Bellaouar, and P. T. Balsara, "IIP2 requirements in 4G LTE handset receivers," in *Proc. 56th Int. Midwest Symp. Circuits Syst. (MWSCAS)*, Aug. 2013, pp. 1132–1135.

[25] *Evolved Universal Terrestrial Radio Access (E-UTRA); User Equipment (UE) radio transmission and reception*, document TS 136 101, V14.3.0, 3GPP, May 2015. [Online]. Available: http://www.3gpp.org/ftp/specs/archive/36_series/36.101/36101-bg0.zip

[26] I. Madadi, M. Tohidian, K. Cornelissens, P. Vandenameele, and R. B. Staszewski, "A high IIP2 SAW-less superheterodyne receiver with multistage harmonic rejection," *IEEE J. Solid-State Circuits*, vol. 51, no. 2, pp. 332–347, Feb. 2016.

[27] K. Dufrene, Z. Boos, and R. Weigel, "Digital adaptive IIP2 calibration scheme for CMOS downconversion mixers," *IEEE J. Solid-State Circuits*, vol. 43, no. 11, pp. 2434–2445, Nov. 2008.

[28] A. V. Oppenheim, R. W. Schafer, and J. R. Buck, *Discrete-Time Signal Processing*, vol. 2. Upper Saddle River, NJ, USA: Prentice-Hall, 1999.

[29] R. Tzschoppe and J. B. Huber, "Causal discrete-time system approximation of non-bandlimited continuous-time systems by means of discrete prolate spheroidal wave functions," *Eur. Trans. Telecommun.*, vol. 20, no. 6, pp. 604–616, Aug. 2008.

[30] D. H. Brandwood, "A complex gradient operator and its application in adaptive array theory," *IEE Proc. F Commun., Radar Signal Process.*, vol. 130, no. 1, pp. 11–16, Feb. 1983.

[31] A. van den Bos, "Complex gradient and Hessian," *IEE Proc.-Vis., Image Signal Process.*, vol. 141, no. 6, pp. 380–383, Dec. 1994.

[32] D. P. Mandic and V. S. L. Goh, *Complex Valued Nonlinear Adaptive Filters: Noncircularity, Widely Linear and Neural Models*, vol. 59. Wiley, 2009.

[33] Y. Chen, T. Le-Ngoc, B. Champagne, and C. Xu, "Recursive least squares constant modulus algorithm for blind adaptive array," *IEEE Trans. Signal Process.*, vol. 52, no. 5, pp. 1452–1456, May 2004.

[34] Y. X. Chen, Z. Y. He, T. S. Ng, and P. C. K. Kwok, "RLS adaptive blind beamforming algorithm for cyclostationary signals," *Electron. Lett.*, vol. 35, no. 14, pp. 1136–1138, Jul. 1999.

[35] A. H. Sayed, *Fundamentals of Adaptive Filtering*, vol. 1. Hoboken, NJ, USA: Wiley, 2003.

[36] P. J. Schreier and L. L. Scharf, *Statistical Signal Processing of Complex-Valued Data: The Theory of Improper and Noncircular Signals*. Cambridge, U.K.: Cambridge Univ. Press, 2010.

[37] R. Isermann, *Identifikation dynamischer Systeme 1 Grundlegende Methoden*, vol. 2. New York, NY, USA: Springer-Verlag, 1991.

[38] R. Ferrús and O. Sallent, *Mobile Broadband Communications for Public Safety: The Road Ahead Through LTE Technology*, vol. 1. Hoboken, NJ, USA: Wiley, 2015.

[39] S. Gunnarsson, "Combining tracking and regularization in recursive least squares identification," in *Proc. 35th IEEE Conf. Decis. Control*, vol. 3, Dec. 1996, pp. 2551–2552.

[40] T. Huckle and M. Sedlacek, "Data based regularization matrices for the Tikhonov-phillips regularization," *PAMM*, vol. 12, no. 1, pp. 643–644, 2012.

[41] J. Dokoupil and V. Burlak, "Variable regularized square root recursive least square method," *IFAC Proc. Volumes*, vol. 45, no. 7, pp. 78–82, 2012.

[42] S. Trampitsch *et al.*, "A nonlinear switched state-space model for capacitive RF DACs," in *IEEE Trans. Circuits Syst. I, Reg. Papers*, vol. 64, no. 6, pp. 1342–1353, Jun. 2017.

Andreas Gebhard (S'16) was born in Bregenz, Austria, in 1982. He received the Dipl.-Ing. degree (Hons.) in electrical engineering from the Graz University of Technology, Graz, Austria, in 2011. His master's thesis was focused on control and automation. His diploma thesis was focused on nonlinear control techniques in cooperation with the Department of Control and Automation. He is currently pursuing the Ph.D. degree at DMCE GmbH & Co KG, as part of Intel within the Christian Doppler Laboratory for Digitally Assisted RF Transceivers for Future Mobile Communications, Linz, Austria.

He was with the Linz Center of Mechatronics, Linz, where he was involved in the research and development of mechatronic systems. Since 2014, he has been a member of the Institute of Signal Processing, Johannes Kepler University Linz, Linz. His current research interests include mitigation of RF impairments using adaptive and statistical signal processing techniques for Long-Term Evolution (LTE) and LTE-A RF transceiver systems.

Oliver Lang (S'14–M'17) was born in Schärding, Austria, in 1987. He received the bachelor's degree in electrical engineering from the Vienna University of Technology, Vienna, Austria, in 2011, and the Ph.D. degree from Johannes Kepler University Linz (JKU), Linz, Austria, in 2018. His master's thesis was focused on the development and analysis of models for a scanning microwave microscope.

He was with the Vienna University of Technology, where he was involved in the study of microelectronics. From 2014 to 2018, he was a member of the Institute of Signal Processing, JKU. Since 2018, he has been with DICE GmbH & Co KG (majority owned by Infineon Technologies), Linz.

Michael Lunglmayr (S'03–M'11) received the Dipl.-Ing. (FH) degree in hardware/software systems engineering from the University of Applied Sciences Upper Austria, Hagenberg, Austria, in 2005, and the Dr.-Ing. degree from the University of Erlangen–Nuremberg, Nuremberg, Germany, in 2009. He is currently pursuing the Ph.D. degree in decoding algorithms for LDPC codes at Infineon Technologies, Munich, Germany.

In 2009, he joined the Embedded Systems and Signal Processing Group, Alpen-Adria Universität Klagenfurt, Klagenfurt, Austria, as a Post-Doctoral Researcher. Since 2014, he has been a Post-Doctoral Researcher with the Institute of Signal Processing, Johannes Kepler University Linz, Linz, Austria, where he became an Assistant Professor in 2016. His current research interests include algorithms for real-time signal processing—especially for estimation—their theory and implementation in digital hardware and software.

Christian Motz (S'17) was born in Vöklabruck, Austria, in 1990. He received the bachelor's degree (Hons.) in hardware software design and the master's degree in embedded systems design from the School of Informatics, Communications and Media, University of Applied Sciences Upper Austria, Hagenberg, Austria, in 2013 and 2015, respectively. His master's thesis was focused on pattern matching cooperation with the Software Competence Center Hagenberg GmbH, Hagenberg. His thesis was on efficient implementation of Weyls discrepancy measure for 2-D image data. He is currently pursuing the Ph.D. degree at the Institute of Signal Processing, Johannes Kepler University Linz (JKU), Linz, Austria, in cooperation with DMCE GmbH (Intel Linz), Linz.

From 2010 to 2015, he was with the University of Applied Sciences Upper Austria. In 2016, he joined the Research Center for Non Destructive Testing GmbH, Linz. Since 2017, he has been a member of the Institute of Signal Processing, JKU, and the CD Laboratory for Digitally Assisted RF Transceivers for Future Mobile Communications, where he is involved in receiver interference cancellation by means of adaptive signal processing methods. His current research interests include LASER-induced ultrasound-based nondestructive material testing.

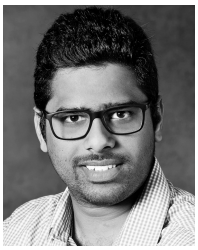

Ram Sunil Kanumalli (S'12) was born in Guntur, India. He received the Dipl.-Ing. (M.Sc.) degree in information technology with a focus on embedded communications and signal processing field from Alpen-Adria-Universitä (AAU), Klagenfurt, Austria, in 2012. He is currently pursuing the Dr.-Ing. (Ph.D.) degree at the Institute of Signal Processing, Johannes Kepler University Linz (JKU), Linz, Austria.

In 2012, he joined the Communications and Signal Processing Group, AAU, as a Research Assistant. From 2013 to 2015, he was a Research Assistant with the Institute of Signal Processing, JKU. Since 2016, he has been with Intel Linz, Linz. His current research interests include the study and development of digital interference cancellation techniques in the presence of various RF imperfections for the next-generation wireless transceiver systems.

Christina Auer (S'18) was born in Linz, Austria, in 1987. She is currently pursuing the Ph.D. degree with Johannes Kepler University Linz (JKU), Linz, in cooperation with DMCE GmbH (Intel Linz), Linz. Her master's thesis was focused on image denoising at the University of California at Los Angeles, Los Angeles, CA, USA.

From 2005 to 2012, she was with JKU, where she was involved in applied mathematics. She was with the Linz Center of Mechatronics, Linz, where she was involved in the research and development, especially with Kalman filtering for localization. Since 2017, she has been a member of the Institute of Signal Processing, JKU, and the CD Laboratory for Digitally Assisted RF Transceivers for Future Mobile Communications. Her current research interests include self-interference cancellation using kernel adaptive filtering.

Thomas Paireder was born in Melk, Austria, in 1992. He received the bachelor's degree (Hons.) in information electronics and the master's degree (Hons.) in electronics and information technology from Johannes Kepler University Linz (JKU), Linz, Austria, in 2016 and 2018, respectively. His master's thesis was focused on signal processing incooperation with the Research Center for Nondestructive Testing GmbH. In his thesis, he implemented a real-time processing system for laser-ultrasonic signals. He is currently pursuing the Ph.D. degree, in cooperation with DMCE GmbH (Intel Linz), Linz, with a focus on receiver interference cancellation by means of adaptive signal processing methods.

From 2012 to 2018, he was with JKU. Since 2018, he has been a member of the Institute of Signal Processing, JKU.

Matthias Wagner (S'18) was born in Linz, Austria, in 1994. He received the bachelor's degree in mechatronics from Johannes Kepler University Linz (JKU), Linz, in 2017. His bachelor's thesis was focused on interference cancellation in automotive FMCW-radar systems, in cooperation with the Institute of Signal Processing, JKU. He is currently pursuing the master's degree in mechatronics with a focus on automation and robotics at JKU.

In 2017, he joined the Institute of Signal Processing, JKU, as a Student Researcher. He is currently with the Christian Doppler Laboratory for Digitally Assisted RF Transceivers for Future Mobile Communications, Linz.

Harald Pretl (S'97–M'01–SM'08) received the Dipl.-Ing. degree in electrical engineering from the Graz University of Technology, Graz, Austria, in 1997, and the Dr.-Techn. degree from Johannes Kepler University Linz (JKU), Linz, Austria, in 2001.

Since 2015, he has been a Full Professor with the Institute for Integrated Circuits, JKU, where he is the Head of the Energy-Efficient Analog Circuits and Systems Group. He is currently a Senior Principal Engineer with the Intel Corporation, Linz, Austria. He has been a Analog Circuit Designer, the Project Lead, the Department Manager, and the RF Systems Architect with the Intel Corporation, where he has been contributing to multiple generations of cellular RF transceivers and mobile communications platforms. He has authored or co-authored more than 40 papers and presentations at international conferences and journals in the area of RF transceivers. He holds more than 25 issued and filed patents. His current research interests include highly integrated GSM/UMTS/LTE/5G transceivers, integrated CMOS power amplifiers for mobile communications and IoT, wireless sensor networks, and low-power RF and mixed-signal SoC.

Dr. Pretl was a member of the Technical Program Committee of the ISSCC from 2010 to 2012. He is a member of the IEEE Solid-State Circuits Society and the Austrian Electrotechnical Association (OVE).

Mario Huemer (M'00–SM'07) was born in Wels, Austria, in 1970. He received the Dipl.-Ing. degree in mechatronics and the Dr.-Techn. degree from Johannes Kepler University Linz (JKU), Linz, Austria, in 1996 and 1999, respectively.

From 1997 to 2000, he was a Research Assistant with the Institute for Communications and Information Engineering, JKU. From 2000 to 2002, he was a Project Manager for DICE Linz GmbH (an Infineon subsidiary), research and development center for wireless products. From 2002 to 2004, he was a Lecturer with the University of Applied Sciences Upper Austria, Hagenberg, Austria. From 2004 to 2007, he was an Associate Professor of electronics engineering, University of Erlangen–Nuremberg, Nuremberg, Germany. From 2007 to 2013, he was a Full Professor of embedded systems and signal processing, Klagenfurt University, Klagenfurt, Austria. From 2012 to 2013, he served as the Dean of the Faculty of Technical Sciences. He is currently the Head of the Institute of Signal Processing, JKU, where he is also a Full Professor. Since 2017, he has been the Co-Head of the Christian Doppler Laboratory for Digitally Assisted RF Transceivers for Future Mobile Communications, Linz. He has authored or co-authored more than 200 scientific papers. His current research interests include statistical and adaptive signal processing, signal processing architectures and implementations, and mixed-signal processing with applications in information and communications engineering, radio frequency and baseband integrated circuits, and sensor and biomedical signal processing.

Dr. Huemer is a member of the IEEE Signal Processing Society, the IEEE Circuits and Systems Society, the IEEE Communications Society, the IEEE Microwave Theory and Techniques Society, the German Society of Information Technology, and the Austrian Electrotechnical Association (OVE).